



NIH Public Access

Author Manuscript

Chem Rev. Author manuscript; available in PMC 2013 May 09.

Published in final edited form as:
Chem Rev. 2012 May 9; 112(5): 2604–2628. doi:10.1021/cr200198a.

UV Resonance Raman Investigations of Peptide and Protein Structure and Dynamics

Sulayman A. Oladepo^{1,†}, Kan Xiong¹, Zhenmin Hong¹, Sanford A. Asher^{1,*}, Joseph Handen², and Igor K. Lednev²

¹Department of Chemistry, University of Pittsburgh, Pittsburgh, PA 15260 USA

²Department of Chemistry, University at Albany, SUNY, 1400 Washington Ave., Albany, NY 12222

1 PROTEIN FOLDING

1.1 The Protein Folding Problem

An understanding of the mechanism(s) of protein folding, whereby the ribosome synthesized biopolymer folds into its native protein is arguably one of the most important unsolved problems in biology.^{1–7} The primary sequence of many or most proteins encodes both the native structure as well as the folding mechanism pathway to the native structure.^{8–10} Over the last fifty years numerous groups have examined the mechanisms of protein folding, with a major objective being to develop methods to predict the native conformation from the primary protein sequence. An understanding of the encoded protein folding “rules” would dramatically speed insight into protein structure and function; this knowledge would result in the first principles design of drugs to treat human diseases, many of which result from protein mutations and/or from protein misfolding.

A vast theoretical and experimental literature exists on protein folding. A number of mechanisms have been proposed that differ in the order of folding events. For example, the framework model¹¹ and the diffusion-collision model¹² propose that the initial step in folding involves formation of native-like secondary structural units, while the hydrophobic collapse model^{13,14} and the nucleation-condensation model¹⁴ suggest that hydrophobic or nucleating domains fold first, and that these structures drive the subsequent formation of secondary structure. Recent energy landscape models^{4,15–24} propose the occurrence of funnel-shaped folding energy landscapes, where the native state is accessed via a strategically sloped energy landscape that funnel myriads of partially folded conformations towards the native folded state.^{4,25,26}

1.2 Techniques for Studying Protein Folding

It is presently impossible to perform first principle simulations of protein folding. The existing theoretical approaches are limited to the modeling of small system dynamics for very short times due to the existing limitations of computer power. The present state-of-the-art modeling utilizes molecular dynamics (MD) with empirical or semiempirical force fields to infer structural and dynamical aspects of protein folding.^{27–29} Unfortunately, computer

*To whom correspondence should be addressed: asher@pitt.edu Phone: 412-624-8570 Fax: 412-624-0588.

†Present Address: Canmet Energy Technology Centre, 1 Oil Patch Drive, Devon, Alberta Canada T9G 1A8

Supporting Information Available

Supporting information associated with this review is available. This information is available free of charge via the Internet at <http://pubs.acs.org/>.

time limitations on the time lengths of the MD simulations prevent straightforward MD calculations to achieve equilibrium structures. Thus, equilibrium structures are generally only inferred from these short MD simulations.

Numerous experimental techniques are being applied to study protein folding. UV-Visible absorption spectroscopy was the first technique used to monitor the UV absorption of the peptide backbone. This method was able to detect protein backbone conformational changes because of the hypo- and hyperchromic interactions that, for example, result from peptide bond excitonic interactions in the α -helix conformation.^{30,31} The development of circular dichroism spectroscopy enabled more direct monitoring of protein secondary structural content, especially the occurrence of α -helical conformations.^{32,33}

X-ray Crystallography is the gold standard technique for determining static protein structures. Unfortunately, its use requires the preparation of protein crystals.³⁴⁻³⁶ Much of the insight into protein science has resulted from the many incisive stationary x-ray structures. However, these static x-ray structures do not give the dynamic structural information essential to determine enzymatic mechanisms, for example. The x-ray structure is used as a basis to infer dynamics. The further the structure of an activated complex from the static structure, the more speculative will be the inference.

Nuclear magnetic resonance spectroscopy (NMR) is an extraordinarily powerful tool for studying protein folding.³⁷⁻³⁹ It can be applied to studying both static structures, and also protein and peptide dynamics. The technique is also capable of elucidating detailed aspects of the structure and dynamics of large proteins. However, the atomic distances and dihedral angles measured by this technique are generally time averages.³⁹ In addition, NMR requires significant measurement time and may require sophisticated isotope labeling. Although, methods based on MD simulation and solid state NMR have been recently developed for the determination of protein conformational distributions in the backbone peptide bonds,^{40,41} information on the distribution of distances and angles about the mean values are crucial for understanding important biological phenomena such as protein folding. Thus, there is a need for spectroscopic methods that give additional insight to investigate protein folding and dynamics.

Optical and especially laser spectroscopy techniques enable highly incisive structural investigations that can be utilized to study dynamics in the fsec to static time scales. IR and Raman vibrational spectroscopies can monitor small changes in protein structure resulting from tiny ~ 0.001 nm bond length changes. Unfortunately, the use of IR absorption spectroscopy is challenging for biological samples, because it is generally limited to D₂O solution samples due to the overwhelming IR absorption of H₂O.⁴²

2. UV RESONANCE RAMAN SPECTROSCOPY

2.1 UV Resonance Raman Scattering

Raman vibrational spectroscopy monitors the vibrations of gas, liquid and solid samples.⁴³⁻⁴⁵ H₂O is a relatively weak Raman scatterer, which enables Raman studies of biological molecules in water. Raman spectroscopy is an inelastic light scattering phenomenon where the incident electromagnetic field interacts with a molecule such that there is an exchange of a quantum of vibrational energy between the two, resulting in a vibrational frequency difference between the incident and scattered light.

The theory of Raman scattering has been well described in the literature.⁴⁶⁻⁵⁵ Fig. 1 compares the IR absorption and Raman scattering phenomena. In IR absorption (Fig. 1a), a molecule absorbs a photon with an energy matching the vibrational energy difference

between two energy levels of a particular molecular vibration. Generally, the molecule undergoes a transition from the $\nu=0$ vibrational ground state to the $\nu=1$ excited vibrational level.

In normal, or off-resonance Raman scattering (Fig. 1b), the incident photon that is at a frequency outside of any electronic absorption band is inelastically scattered, leaving the molecule in an excited vibrational level of the electronic ground state (for Stokes scattering). An identical vibrational transition occurs for resonance Raman scattering, where excitation occurs at a frequency within an electronic absorption band (Fig. 1c). In this case the vibrational modes observed are particular vibrations whose motions couple to the driven electronic motion occurring in the electronic transition. The vibrational modes enhanced are those localized in the chromophoric segments. The resonance Raman cross sections are much larger than the nonresonance Raman cross sections.

As for any light scattering process from objects significantly smaller than the wavelength of light, the Raman intensities increase approximately with the fourth power of the excitation frequency. The additional *resonance* Raman enhancement can be an additional 10^6 - 10^8 -fold. This results in a crucial ultra-high resonance Raman selectivity and sensitivity that makes it a very powerful technique for studying macromolecules. Instead of all the sample vibrations contributing with comparable intensities, only a small set of resonance Raman enhanced vibrations localized around the chromophoric group dominate the spectra.

Judiciously tuning the excitation wavelength, allows for selectively enhancing a particular vibrations in particular regions of the macromolecule.^{56,57} Fig. 2 demonstrates the UV resonance Raman (UVRR) selectivity available, for example, for studying the protein myoglobin (Mb).^{58,59} The visible wavelength absorption bands of Mb result from the in-plane $\pi \rightarrow \pi^*$ electronic transitions of its heme group. UVRR excitation of Mb at 415 nm in the strong heme Soret absorption band, results in an intense UVRR spectra which contains only the in-plane heme ring vibrations.^{60,61} In contrast, excitation at 229 nm within the absorption bands of the tyr and trp aromatic side chains shows UVRR spectra completely dominated by tyr and trp aromatic ring side chain vibrations.⁶² Deeper UV excitation at 206.5 nm, within the $\pi \rightarrow \pi^*$ transitions of the amide peptide bonds, shows UVRR spectra dominated by the peptide bond amide vibrations.⁵⁹

Thus, tuning the UVRR excitation wavelengths, allows the probing of different chromophoric segments of a macromolecule. Another advantage of deep UV Raman measurements is that there is no interference from molecular relaxed fluorescence since those chromophores that have their first transition below 260 nm are highly flexible and possess vanishingly small fluorescence quantum yields.⁶³ In addition, UVRR can also be used in pump-probe measurements to give kinetic information on fast biological processes.^{64,65} Thus, UVRR is a powerful technique for studying static protein structure and for studying protein dynamics, such as, for example, in protein folding.

2.2 UV RR Instrumentation

The rapid development of UVRR has been aided by recent advances in lasers, optics and detectors. Fig. 3 shows the schematic diagram of a typical back scattering UVRR instrument that can be used for static and kinetic studies.⁶⁶⁻⁶⁹ For temperature-jump (T-jump) measurements an IR pump pulse at $1.9 \mu\text{m}$ excites the overtone absorption band of water and heats a small sample volume. A time delayed UV probe pulse excites the UVRR of the IR pulse heated volume. The UVRR light is collected and dispersed by a spectrograph and the spectrum is detected by a CCD detector. Non kinetic Raman measurements of static structure are best measured by using CW lasers that avoid nonlinear optical processes and thermal processes that can induce sample degradation.⁷⁰⁻⁷²

However, high repetition rate (1-5 KHz) pulsed (10-50 nsec) Nd:YLF pumped Ti:Sapphire lasers^{67,73} are very convenient UVRR laser sources because their output can be easily and continuously tuned between 193 nm to 240 nm. These deep UV excitation beams are generated by frequency quadrupling or tripling and mixing the Ti:Sapphire laser fundamentals.

UVRR measurements generally flow the sample through the excitation beam as shown in Fig. 3 to avoid sample heating and accumulation of photochemical degradation products. Excitation of an open sample stream sample also avoids any interfering Raman signals from sample cell walls.⁷⁴ If the sample volume is limited, a spinning silica capillary or cuvette with a magnetic stir bar can be used to contain the sample.^{67,75}

Liquid nitrogen cooled CCD cameras are the optimum UVRR detectors because of their low noise. At present the best S/N comes from CCD cameras with fluorophore coatings to convert the UV light into the visible where the CCD detector has high quantum efficiencies.

3. PROTEIN AND PEPTIDE BOND STUDIES

Fig. 4a shows the HOMO and LUMO molecular orbitals of the peptide bond (secondary amide group, except for proline). The lowest energy $n \rightarrow \pi^*$ transition at ~220 nm is electronically forbidden and weak. It gives rise to the strong CD signature of the α -helix conformation but gives rise to negligible RR enhancement.^{76,77} The ~190 nm $\pi \rightarrow \pi^*$ transition is strongly allowed, with a strong absorption band that gives rise to strong UVRR intensities.⁷⁸ This electronic transition results in a significant expansion of the C-N bond with a smaller expansion of the carbonyl bond. Excitation within this absorption band gives rise to the strong UVRR enhancement of vibrations that have large components of C-N stretching. A somewhat smaller enhancement occurs for vibrations with a large component of C=O stretching.⁷⁹

Fig. 4b-e show the UVRR peptide bond vibrations enhanced. Excitation at ~200 nm gives rise to strong UVRR intensities for particular peptide bond vibrations,^{75,80-84} that include: the Amide I (AmI) vibration (~1660 cm⁻¹) that consists mainly of C=O stretching and a small amount of out-of-phase C-N stretching; the Amide II (AmII) vibration (~1550 cm⁻¹) that consists of an out-of-phase combination of CN stretching and NH bending motions; and the Amide III (AmIII) vibration (between ~1200 - 1340 cm⁻¹) which is a complex vibration involving C-N stretching and NH bending. An AmIII vibration that contains significant C_α-H bending (~1390 cm⁻¹) is also enhanced if the peptide bond conformation enables C_α-H bending motion to couple to C-N stretching.⁸⁵

These UVRR enhanced peptide bond vibrations (except for the AmI) derive from vibrational modes localized within individual peptide bonds. The AmI vibrations show small couplings between adjacent peptide bonds.^{80,86,87} The local mode character of the Am II, AmIII and C_α-H bending peptide bond vibrations allows the measured UVRR spectrum to be modeled as the linear sum of contributions of the individual peptide bond UVRR spectra.⁸¹

This enabled Asher and coworkers to develop a quantitative methodology to determine protein secondary structure directly from the measured UVRR spectra.⁸⁸ They measured the UVRR spectra of a set of proteins with known x-ray structures and calculated the “basis” spectra of the three major secondary structure motifs: the α -helix, β -sheet and unfolded conformation.

Fig. 5 shows the basis spectra of the α -helix, β -sheet and unfolded structures obtained as discussed above. The pure α -helix spectrum shows an AmI band at 1647 cm⁻¹, an AmII band at 1545 cm⁻¹, an AmIII band at ~1299 cm⁻¹ and no C_α-H bending band. The pure β -

sheet spectrum shows an AmI band at 1654 cm^{-1} , an AmII band at 1551 cm^{-1} , an AmIII band at 1235 cm^{-1} and the $\text{C}_\alpha\text{-H}$ bending band at 1386 cm^{-1} . The unfolded structure (now known to be PPII) spectrum shows an AmI band at 1665 cm^{-1} , an AmII band at 1560 cm^{-1} , an AmIII band at 1267 cm^{-1} and a $\text{C}_\alpha\text{-H}$ bending band at 1386 cm^{-1} .⁸⁸ The fractional secondary structure composition of a protein with an unknown secondary structure can be uniquely determined by linearly fitting these basis spectra to the protein UVRR. The fitted weighting fractions are the fractional amounts of each secondary structure motif.⁸⁸

3.1 UVRR Excitation Profiles

RR excitation profiles, which display the dependence of the resonance Raman cross sections on the excitation wavelength, detail the magnitude of coupling of vibrations to the electronic transitions underlying the absorption band envelope. UVRR excitation profile measurements and measurements of the wavelength dependence of the Raman depolarization ratios (ρ) provide information on the underlying electronic transitions that are responsible for the broad complex absorption bands. Fig. 6 shows the UVRR spectra of the α -helix and the melted, PPII conformations of a 21-residue mainly ala peptide (AP) of sequence, AAAA(AAARA)₃A excited between 218 nm and 194 nm.⁷⁷ The relative intensities of the Raman bands increase as the excitation wavelength decreases from 218 to 194 nm. The UVRR excitation profiles of different conformations differ, as do their UVRR spectra as discussed in detail below.⁷⁷ The UVRR cross sections for the PPII-like conformation are approximately twice those of the α -helical conformation (for $\lambda > 200\text{ nm}$, Fig. 7) due to the hypochromism that results from the excitonic interactions between the α -helical peptide bond electronic transitions.

The α -helix and the melted PPII conformations also show different excitation profile maxima, indicating shifts in absorption band maxima between the underlying electronic transitions. A shoulder seen in the excitation profiles (Fig. 7) around 206 nm suggests an additional underlying electronic transition, which is confirmed by the complex dispersions of the depolarization ratios, that otherwise would have a value $\rho = 0.33$ if derived from a single nondegenerate electronic transition.^{46,77} In a related study,⁸⁹ the excitation profiles of tri- and tetraalanine peptides revealed 202 nm charge transfer electronic transitions, where electron transfer occurs from the terminal nonbonding carboxylate orbital to the adjacent peptide bond π^* orbital,⁸⁹ as observed previously for glycylglycine.⁹⁰ From this work it is clear that there presently exists only a modest understanding of the UV electronic transitions of peptide bonds.

3.2 Correlation Between Spectral Features And Protein Secondary Structure

The UVRR spectra of proteins and peptides are conformationally sensitive as shown in the Fig. 8 UVRR study of α -helix melting of poly-L-glutamic acid (PGA) at pH 4. PGA is α -helical at low temperatures, but melts to unfolded structures at high temperatures.⁹¹ The α -helix low temperature UVRR spectrum shows an AmI band at $\sim 1647\text{ cm}^{-1}$, an AmII band at $\sim 1560\text{ cm}^{-1}$, a ($\text{C}\text{C}_\alpha\text{-H}$) bending band (also called the Am S band by some workers) at $\sim 1390\text{ cm}^{-1}$, and AmIII bands between $\sim 1200\text{ cm}^{-1}$ and $\sim 1340\text{ cm}^{-1}$. As the temperature increases, the AmI band upshifts from $\sim 1647\text{ cm}^{-1}$ to $\sim 1670\text{ cm}^{-1}$ and becomes broader, while the AmII band downshifts from $\sim 1560\text{ cm}^{-1}$ to $\sim 1555\text{ cm}^{-1}$. These results indicate weakened hydrogen bonding (HB) with increasing temperature. Previous work showed that the water HB to the peptide bond C=O increases the C=O bond length and, thus, downshifts the AmI band, while water HB to the peptide bond N-H upshifts the AmII band.⁹² Thus, the extent of HB partially determines the UVRR band frequencies (see a discussion of different HB patterns below).

The C_α-H intensity increase with temperature indicates α -helix melting.^{85,88} The α -helix conformation shows a negligible C_α-H bending band intensity, in contrast to the unfolded extended conformation that has a high C_α-H bending intensity.^{85,88}

The AmIII region contains three sub-bands: AmIII₁, AmIII₂ and AmIII₃. However, only two of these sub-bands are clearly resolved in the AmIII region of PGA: the AmIII₂ band ($\sim 1303\text{ cm}^{-1}$) and the AmIII₃ band ($\sim 1250\text{ cm}^{-1}$). The AmIII₃ band (that is most sensitive to conformation), derives from motions that involve coupling of NH bending to C_α-H bending and CN stretching.^{83,93} As the temperature increases, the melted polyproline II (PPII)-like conformation increases and the corresponding unfolded PPII AmIII₃ band ($\sim 1247\text{ cm}^{-1}$) in PGA becomes more prominent, overshadowing the low temperature α -helical AmIII₃ band. This clearly signals melting of the α -helix conformation to a PPII conformation.

The large AmIII₃ band frequency conformational dependence derives from the fact that coupling between C_α-H bending and N-H bending peptide bond motions depends sensitively on the peptide bond Ramachandran Ψ dihedral angle that, in part, defines the peptide bond secondary structure conformation.^{82,91}

The Asher group discovered a sinusoidal dependence of the AmIII₃ frequency on this Ramachandran Ψ angle.^{82,91} Conveniently, they also found little dependence of the AmIII₃ frequency on the other dihedral angle, the Ramachandran Φ angle (for sterically allowed Ψ angles).⁹⁴ The origin of this Ψ angle frequency difference between the α -helix and extended conformations results from the fact that the α -helix peptide bond conformations have *cis* N-H and C_α-H bonds that prevent coupling (Fig. 9). Thus, the α -helix AmIII₃ frequency occurs at 1258 cm⁻¹ and the C_α-H bending band contains negligible C-N and N-H bending motion, and is, thus, not resonance enhanced.

In contrast, peptide bonds adopting an extended PPII-like conformation have *cis* N-H and C_α-H bonds whose motions couple well. The AmIII₃ band frequency downshifts to 1245 cm⁻¹ and the C_α-H bending vibration contains C-N stretching and N-H bending motion resulting in resonance enhancement.⁸² Quantitative relations were determined that relate the AmIII₃ band frequencies to Ramachandran Ψ angles for different peptide bond HB states.⁸²

For example for peptide bonds fully hydrogen bonded to water such as in PPII, 2.5₁-helix, and extended β -strand conformations:

$$\nu_{AmIII_3}^{EXT}(\Psi, T) = 1256 \text{ cm}^{-1} - 54 \text{ cm}^{-1} \cdot \sin(\Psi + 26^\circ) - 0.11 \frac{\text{cm}^{-1}}{\text{^oC}} T \quad (1)$$

where T is temperature. The family of quantitative relationships determining the AmIII₃ frequencies ignore the more modest Ramachandran Φ angle dependencies.⁹⁴

This family of equations allows estimation of the Ψ angle for the different possible peptide bond HB states. The estimated error of this determination was suggested to be $\pm 14^\circ$.⁸² Fig. 10 shows the family of theoretical curves that correlate the AmIII₃ frequencies to the Ramachandran Ψ angles for the different HB states.⁸² As shown below, correlating the inhomogeneously broadened AmIII₃ bandshape to the underlying Ramachandran Ψ angle distribution enables the determination of the peptide bond conformational distributions in peptides and proteins. Most importantly, these conformational distributions can be used to calculate the Gibbs free energy landscapes along the Ψ angle coordinates, which are the most important (un)folding reaction coordinates.

3.3 Protein Folding Energy Landscapes

The UVRR spectra show inhomogeneously broadened bands that reflect the distribution of conformations experienced by the protein. In the case of the AmIII₃ band the inhomogeneous distribution reflects mainly the distribution of peptide bond Ψ angles and HB states.

Asher and coworkers assumed that the experimentally measured, inhomogeneously broadened AmIII₃ band, $A(\nu)$ derives from the sum of M Lorentzian bands which result from the different peptide bond conformations with different band frequencies, νe_i . The AmIII₃ band homogeneous linewidth, $\Gamma = 7.5 \text{ cm}^{-1}$ was determined from UVRR measurements of small peptide crystals in defined secondary structure states.⁹⁵

$$A(\nu) = \pi^{-1} \sum_{i=1}^M L_i \cdot \frac{\Gamma^2}{(\nu - \nu e_i)^2 + \Gamma^2} \quad (2)$$

where L_i is the probability for the contributing band to occur at frequency νe_i .

Asher and coworkers deconvoluted out the homogeneous linewidth from the peptide bond UVRR spectrum to calculate the underlying inhomogeneously broadened AmIII₃ band shape.⁹⁵ Fig. 11 shows histogram plots of the calculated underlying AmIII₃ band frequency distributions for a set of peptides and proteins. The XAO peptide of sequence Ac-XXAAAAAAOO-NH₂ (A is alanine, O is ornithine, X is diaminobutyric acid) is known to be primarily in a PPII conformation.⁹⁶ As shown in Fig. 11, the XAO frequency distribution is similar to that of A₅-A₃ (the difference UVRR between ala₅ and ala₃ that models the spectrum of the interior A₅ peptide bonds), indicating that these peptide bonds predominantly populate the PPII conformation, as do the peptide bonds of the AP peptide (primarily polyala) at elevated temperature. Acid-denatured apomyoglobin shows a broad frequency distribution, as expected, from its distribution of conformations. The “protein library”, of course, shows the broadest frequency distribution.

Asher and coworkers used eq. 1, relating the AmIII₃ band frequency to the Ramachandran Ψ angle, to convert the frequency distributions to Ψ angle distributions (Fig. 12). Further, by applying the Boltzmann relation to the Ψ angle distributions, the relative Gibbs free energy along the Ramachandran Ψ angle coordinate can be calculated, since the population at any particular Ψ angle is determined by its relative Gibbs free energy.⁹⁷

For example, this approach was used to determine the Gibbs free energy landscape (Fig. 13) for Poly-L-lysine (PLL). At neutral and low pH values, PLL adopts extended conformations that include the PPII and 2.5₁-helix conformations. The 2.5₁-helix conformation results from the PLL charged side chains electrostatic repulsions.^{97,98} Ma et al.⁹⁹ used UVRR to monitor the temperature and NaClO₄ concentration dependence of the PLL Gibbs free energy landscape (Fig. 13). They observed an α -helix-like basin containing α -helix and π -bulge conformations and a basin containing PPII and 2.5₁-helical extended conformations.

As indicated in Fig. 13, adding NaClO₄ induces a change from a solution equilibrium between extended PPII and 2.5₁-helical conformations, to an equilibrium involving α -helix-like conformations.⁹⁹ This conformational change results from charge screening due to strong ion-pair formation between ClO₄⁻ and the lysine side chain $-NH_3^+$, that reduces the repulsion between charged side chains. Fig. 13 also shows that increasing temperatures cause the α -helix-like conformations to melt to extended conformations.

3.4 T-Jump Kinetic Studies of Protein Folding

Dynamic UVRR measurements can be used to elucidate biomolecular structural dynamics.⁵⁴ T-jump experiments monitored by UVRR measurements can elucidate the evolution of peptide and protein secondary structure.^{42,69,84,100-109} These studies probe the mechanism of structural evolution between different secondary structural motifs such as α -helix, 3_{10} -helix, π -bulge and PPII conformations.^{42,84,100-103,110} The rates of these transitions occur in the 100 nsec to $\sim 2 \mu\text{sec}$ time regime.

Recent nsec to μsec protein folding dynamics studies found complex unfolding behaviors. For example, recent studies of the AP peptide melting demonstrate a complex pathway that involves melting of multiple α -helix-like structures, which include the 3_{10} -helix, π -bulge and pure α -helix conformations that have different melting curves to the PPII-like unfolded conformation.^{82,84,101,111}

To gain insight into the dynamics of protein (un)folding, the Asher group constructed the first T-jump UVRR spectrometer that they used to examine conformational relaxation subsequent to nsec T-jumps.^{84,101} The peptide and protein relaxation after the T-jump utilizes folding and unfolding conformational change coordinates that are easily studied with UVRR. These T-jumps used ~ 5 nsec, excitation pulses at $1.9 \mu\text{m}$ that occur within a water vibrational overtone absorption band. Thermalization of the absorbed energy occurs within 70 ps.^{112,113} It is easy to achieve $\sim 20^\circ\text{C}$ T-jumps from the ~ 5 nsec IR laser pulses.

In their first kinetic studies, the Asher group examined the kinetics of melting of the AP peptide that at low temperature is mainly α -helical.¹⁰¹ Steady state measurements discussed above showed that the α -helix melts to a PPII conformation. Fig. 14A shows the T-jump relaxation transient difference UVRR spectra of AP in H_2O and D_2O . The transient difference spectra measured at delay times as long as 1 sec were modeled using a linear combination of α -helix and the PPII equilibrium UVRR basis spectra. The first spectral changes evident at <10 nsec derive from fast HB changes of water bound to the peptide bonds in the PPII state due to the temperature increase.¹⁰⁰

Subsequent relaxation spectral changes result from peptide bond conformation changes. Modeling of the transient spectra can determine the kinetics of the AP structural relaxation. Depending on the initial temperature, unfolding time constants between 180 and 240 ns were observed. By assuming a 2-state model they calculated a folding time constant of $\sim 1 \mu\text{s}$ (Fig. 14).^{84,100,101}

They also observed a puzzling peculiarity in the temperature dependence of the folding and unfolding rate constants that they calculated from the relaxation rates by assuming a 2-state system (that was fully consistent with the observed single exponential relaxation behavior). As the temperature increased, they calculated that the folding rate constant decreased, indicating a negative activation energy of $-4^{+3}_{-2} \text{ kcal/mol}$, that indicates an anti-Arrhenius behavior.¹⁰¹ Obviously, this peculiarity must result from the fact that the conformational transition is not 2-state.

Subsequently, Mikhonin et al. identified the additional states involved in the melting transition.¹¹¹ They found that they could spectrally differentiate α -helix-like conformational substates from the AmIII_3 band frequency distribution.¹¹¹ They calculated the α -helix-like UVRR spectrum by subtracting off the pure PPII UVRR spectrum measured at higher temperature (after accounting for the temperature dependence of the PPII UVRR spectrum). Fig. 15 shows calculated Ramachandran Ψ angle distributions in AP between 0 $^\circ\text{C}$ and 30 $^\circ\text{C}$.

At low temperatures, the Ψ angle distribution of the α -helix-like state is broad and spans the Ψ angles of the pure α -helix, 3_{10} -helix and π -helix bulge conformations. As the temperature increases the α -helix-like Ψ angle distribution narrows until at 30 °C, the distribution becomes very narrow and centered at -42°, the Ψ angle of the pure α -helix.

Fig. 16 shows the melting curves determined for these different α -helix-like conformations by assuming identical Raman cross sections for the pure α -helix, the 3_{10} -helix and the π -bulge conformations. T_m was determined to be 45 °C, 20 and 10 °C for the α -helix, 3_{10} -helices and π -bulges, respectively.

The anti-Arrhenius behavior observed by Lednev et al.'s T-jump measurements directly results from these different T_m for the 3_{10} -helix, π -bulge and pure α -helix conformations.¹⁰⁷ As the temperature increases the pure α -helix conformation increasingly dominates the equilibrium conformational distribution. Apparently, the folding rate of the pure α -helix conformation is slowest. These studies clearly show the utility of UVRR to gain crucial insight into the complex nature of peptide folding dynamics.

In a recent protein T-jump study, Spiro et al.¹⁰⁴ examined the early events in the unfolding of apomyoglobin using both 197 and 229 nm excitation. These excitations allowed them to probe both the aromatic side chains and the peptide backbone conformations. Aromatic amino acid side chain UVRR bands can monitor the solvent exposure, while the peptide bond UVRR bands report on backbone Ramachandran Ψ angles, as discussed above. Measuring both spectral bands can answer the question of whether solvent exposure of the protein core precedes or follows secondary structure changes. The authors were able to clearly differentiate the order of these events. They found that the Trp14 bands respond twice as fast as does the peptide bond α -helix melting. Thus, the Trp14 that is originally buried in the protein core, becomes exposed to solvent, prior to melting of the protein core.

In another T-jump study,¹⁰⁶ the Spiro group found two relaxation time constants of 0.2 and 15 μ s for a truncated version of the GCN4 coiled-coil peptide. They interpreted that their UVRR spectra revealed two different α -helical AmIII bands at 1340 and 1300 cm^{-1} that melt at 10 and 40 °C, respectively. The authors argued that these two bands and their different time constants reflect the melting of hydrated and unhydrated helices in the folded polypeptide chain. This is the first report of the differentiation of hydrated and unhydrated helices from UVRR.¹⁰⁶

The Spiro group also found two distinct kinetic phases for the melting of the α -helical peptide (AcGSPEAAKAKAAA-CO-D-R-CONH₂).¹⁰⁵ They observed a prompt loss of helicity (within the ~40 ns time resolution of the experiment), whose amplitude increased with the increasing final T-jump temperature, T_f . With a constant initial temperature, T_i , the amplitude of the fast phase is initially small for small T-jumps, but increases as T_f increases from 18–61 °C. However, when T_i is raised in parallel with T_f the fast phase merged into the slow phase (120 ns). They claimed that this merging of fast and slow phases is due to the shifting distribution of initial helix lengths from longer to shorter helices as the T_i - T_f range shifts to higher temperatures. These two relaxation phases were attributed to a fast disruption of HB followed by slower peptide bond conformational changes. The fast (~40 ns) conformational change kinetics are quite surprising. Understanding these apparently complex dynamics will require additional studies.

3.5 Isotope-Labeling Enables Monitoring of Secondary Structure Spatial Distributions

Ianoul et al. used UVRR to examine the spatial dependence and the thermodynamics of α -helix melting of deuterium labeled AP (AdP).¹¹⁰ In AdP, all the ala residues except the four central ones were selectively deuterated. They found that melting of the isotopically labeled

exterior peptide bonds could be spectrally resolved from the central ones; thus allowing the spatial resolution of the peptide bond conformational changes. The UV Raman spectra of AP and AdP at 5 °C are compared in Fig. 17A. Fig. 17B shows that the central residues are essentially 100 % α -helix-like at 0 °C with a T_m of 32 °C while the exterior residues are ~60 % α -helix-like at 0 °C with a T_m of 5 °C.

For a 5 to 30 °C T-jump, the central peptide bonds show a ~2-fold slower relaxation time of 189 ns, compared to 97 ns for the exterior peptide bonds.¹⁰⁷ However, for a 20 to 40 °C T-jump, the central peptide bond relaxations are faster (56 ns), than those of the exterior peptide bonds (131 ns). Assuming a two-state transition, only the exterior peptide bonds show anti-Arrhenius behavior; the central peptide bonds show both normal Arrhenius-like folding and unfolding.

They ascribed the anti-Arrhenius folding behavior of the exterior peptide bonds to the involvement of π -bulges/helices and 3_{10} -helix states in unfolding.¹⁰⁷ Since these α -helix-like motifs have a lower T_m than that of the pure α -helix,¹¹¹ large relative contribution from lower melting 3_{10} -helices and π -bulges/helices should give faster relaxation kinetics. In contrast, a large relative contribution from the higher melting pure α -helix conformation should give slower relaxation kinetics. Hence, the authors explained that the central peptide bonds show a ~2-fold slower relaxation kinetics in the 5 to 30 °C T-jump, because of a higher contribution to the relaxation by the slower pure α -helix relaxation compared to that of the exterior peptide bonds (27% vs -3%). For the 20 to 40 °C T-jump, the central peptide bonds show faster relaxation kinetics because of the lower contribution to the relaxation by the slower pure α -helix relaxation compared to the exterior peptide bonds (7% vs 35%). The small relative contribution of the pure α -helix conformation to the central peptide bonds results in a faster relaxation.

The results obtained from this work are obviously complex. The authors argued that the results can only be understood by assuming that one of the AdP termini has a higher pure α -helix propensity than the center and the other terminus. They proposed that the pure α -helix is most stabilized at the N-terminus where eight consecutive ala occur than at the middle and C-terminus.¹⁰⁷ This study clearly shows that UVRR can spatially resolve the melting dynamics of peptides and proteins.

3.6 UVRR of Side Chains as Spectral Monitors of Protein Structure

Aromatic amino acid side chain chromophores show strong UVRR spectra upon 229 nm excitation (Figure 2). UVRR aromatic amino acid studies have been extensively used to monitor different aspects of protein structure. For example, Hashimoto, et al. used UVRR excitation at 229 nm to examine the acid-induced unfolding intermediates of sperm whale apomyoglobin and metmyoglobin.¹¹⁴ They monitored the W3 and W7 band changes associated with Trp7 and Trp14 residues to probe the pH-dependent structural protein changes. They found that the unfolding of myoglobin is accompanied by a significant decrease in environmental hydrophobicity around the Trp residues. They also found that the fully unfolded form partially refolds in the presence of sulfate ions.¹¹⁴ Their results also suggest a two-step transition from the native to the unfolded conformation for both proteins. These results are consistent with the two unfolded intermediates found earlier for horse apomyoglobin by Chi et al.¹¹⁵ They argued that the transition from the native form to the unfolding intermediate results from an increased water exposure of Trp14 that is close to the E helix. This conclusion is based on a previous report by Hughson et al. that the intermediate form of apomyoglobin has an unfolded E helix.¹¹⁶ However, this conclusion contrasts with the increased water exposure of Trp7 identified by Chi et al.,¹¹⁵ that was also corroborated by Haruta's time-resolved UVRR experiments.¹¹⁷

In a pH-jump kinetic UVRR study, Haruta et al. characterized the kinetic folding intermediates of horse apomyoglobin (h-apoMb), using a rapid mixer.¹¹⁷ Similar to Hashimoto's kinetic study, they monitored changes in W3 and W7 bands of Trp7 and Trp14. The pH-dependence of the intensity ratio of the W7 doublet (I_{1358}/I_{1338}) indicates the presence of two transitions; a transition between the native and equilibrium intermediate state and a transition between the equilibrium intermediate and unfolded states. In addition, analysis of their measured 244 nm excited UVRR spectra at different delay times following a pH-jump from pH 2.2 to pH 5.6 reveals three folding intermediates, I₁, I₂ and I₃. They found that the first intermediate formed before the earliest delay time of 0.25 ms. They were able to detect this intermediate by observing an upshift in the W3 band from 1553–1557 cm⁻¹ at 0.25 ms after acid unfolding.

They rationalized this observation from experiments with a model peptide of the A helix in water and in helix-forming solvents (e.g. trifluoroethanol/methanol/water mixture). The W3 band occurs at 1552 and 1555 cm⁻¹ in water and in helix-forming solvents, respectively. They therefore concluded that I₁ involves the incorporation of Trp14 into the α -helix from the acid-induced random coil. The second intermediate, that formed 1 ms after the start of refolding, indicates decreased water exposure whereby the surroundings of Trp7 and Trp14 are hydrophobic. The third intermediate appeared at ~3 ms. From the I_{1358}/I_{1338} vs time plot, the hydrophobicity of the system at this stage is equal to that obtained for a pH 4 equilibrium intermediate. They also found that an upshift in the W3 band frequency did not occur even 40 ms after the pH-jump. Thus, they concluded that the transition from I₃ to the native state took more than 40 ms, indicating a slow process. This kinetic study presents a direct observation of the structural and environmental changes in the Trp side chain of h-apoMb in its early stage of refolding from an almost completely unfolded structure.

In another study, Sato et al. used time-resolved UVRR spectroscopy to probe the structural dynamics of myoglobin following carbon monoxide (CO) dissociation.¹¹⁸ Their ps transient UVRR spectra showed transient intensity changes for the Trp W18, W16 and W3 bands and the Tyr Y8a band that resulted from changes in the heme structure upon CO dissociation. They argued that out-of-plane motion of iron following CO dissociation induces protein motion such as E and F helical movements. They observed decreased intensities for these Trp and Tyr bands within 5 ps of CO dissociation. They explained that this decreased intensities resulted from rapid movement of both E and F helical segments. The occurrence of decreased intensity within 5 ps implies that the concerted EF helical movement following CO dissociation is ultrafast.¹¹⁸ The myoglobin protein response due to CO dissociation is demonstrated in this study.

Kim's research group examined the folded and unfolded states of the wild type bacterial outer membrane protein A (OmpA) and two OmpA mutants.¹¹⁹ Using 230 nm excitation, they studied these proteins in the absence of urea (folding condition) and in the presence of urea (unfolding condition). Under *in vitro* folding and unfolding conditions, they probed the Trp and Tyr side chain environments to monitor OmpA folding and unfolding. Based on changes in the W7 doublet intensity ratio (I_{1361}/I_{1340}) as well as shifts in W3 and W17 bands, they found that an OmpA mutant (W57 OmpA) is folded in vesicles and in detergent, but unfolded in phosphate buffer. This work presents a UVRR spectral investigation of an integral membrane protein that is folded in a synthetic bilayer vesicle and uses the changes in the Trp and Tyr environments to delineate structural protein changes.

El-Mashtoly et al. used UVRR spectroscopy to examine the Trp and Tyr bands to probe the structural changes that accompany the photocycle of the photoactive yellow protein (PYP).¹²⁰ PYP is a bacterial blue light photoreceptor. Photoexcitation of its dark-state (PYP_d) triggers a photocycle that involves a number of intermediate states that leads to the

formation of the putative signaling state (PYP_m). With 225-250 nm UV excitation, the authors observed shifts and intensity changes in Tyr Y8a and Y9a bands that they attributed to HB changes between the Tyr42 and the chromophore in PYP_m . They also observed a decreased intensity of the Trp W3, W16 and W18 bands upon PYP_m formation. These decreases in intensity are ascribed to an increased water exposure of the only Trp in PYP (Trp119) that is located more than 10 Å from the protein's active site. They therefore concluded that these observed changes suggest global protein structural changes during the transition from PYP_d to PYP_m .¹²⁰ The study gives structural insight into the photocycle of the bacterial blue light photoreceptor, PYP.

Mathies research group used picosecond time-resolved UVRR spectroscopy to probe the structural dynamics of rhodopsin.¹²¹ In this study, they used a pump-probe apparatus consisting of a 1 kHz Ti:Sapphire laser system that provides <3 ps pump (466 nm) and probe (233 nm) pulses. They monitored Trp and Tyr spectral features in order to probe rhodopsin structural changes following photon absorption. With 233 nm probe pulses, they observed a decreased Raman intensity in the Trp W3, W16 and W18 bands at zero time delay between pump and probe events. However, at longer time delays, they found that both the Trp W1, W3, W16 and W18 bands and the Tyr (Y1+2xY16a Fermi doublet, Y7a and Y8a) bands show decreased intensities. These intensity changes are attributed to a decreased hydrophobicity of the microenvironment of at least one Trp and one Tyr. Examination of the rhodopsin crystal structure suggests that W265 and Y268 are responsible for the observed UVRR spectral changes. These spectral changes are nearly identical to those observed for the transition in rhodopsin to the 1 ms intermediate (Meta I). These similarities suggest that Trp and Tyr spectral changes that lead to Meta I are initiated very early in the process, perhaps 200 fs following photon absorption. They therefore concluded that the Trp and Tyr structural changes in rhodopsin dynamics were initiated as early as 200 fs into the photoisomerization process. This study gives temporal glimpses into the structural changes that accompany the primary photochemical event in vision.

The Mathies group also carried out time-resolved UVRR experiments to characterize the structural changes that take place in the photochemical reaction cycle of bacteriorhodopsin.¹²² This study carried out with 239.5 nm excitation showed Trp W1, W3, W16 and W18 intensity decreases and an upshift in the Tyr Y8b band in their 10 ns transient difference spectra. These observed spectral changes suggested that the photoisomerization of retinal from all-*trans* to 13-*cis* changes the structure and environment of aromatic residues that line the retinal binding pocket within 10 ns following photo absorption. This study reveals that UVRR spectroscopy can give insight into the early part of the photochemical cycle of membrane proteins such as bacteriorhodopsin.

Barry and coworkers used pump-probe UVRR to study the roles of Trp and Tyr in electron transfer in photosystem II (PSII) in the photosynthesis process.^{123,124} They used 633 nm light to initiate the photochemistry and 244 and 229 nm light to probe the conformations of Trp and Tyr. They observed light-induced Tyr radical Z· and/or Tyr radical D· intermediates, as well as plastoquinone anions Q_A⁻, Q_B⁻ during electron transfer in PSII.

Okishio, et al. used 235 nm UVRR excitation to probe the effect of tyrosine phosphorylation in Src-peptides (RRLIEDNEYTARG and TSTEPQYQPGENL).¹²⁵ Upon tyrosine phosphorylation, they observed that the Y8a band downshifts from 1615 cm⁻¹ to 1611 cm⁻¹ while the Y7a' band downshifts from 1250 cm⁻¹ to 1240 cm⁻¹. They also observed a diminished intensity of the Y1 band at around 850 cm⁻¹ and the appearance of the Y13 band at around 760 cm⁻¹. When they dephosphorylated the initially phosphorylated peptides with alkaline phosphatase (an enzyme that removes phosphates from proteins), they found that the phosphorylation-induced changes disappeared. Thus, UVRR spectroscopy can be used to

delineate structural changes caused by protein phosphorylation and other protein modifications.¹²⁵

3.7 Other UVRR Protein Studies

The Spiro group used UVRR spectroscopy to establish quantitative signatures of protein secondary structure via least-square fitting,⁷⁴ following the example of the method reported by Chi et al.⁸⁸ They used 197 and 206.5 nm excitation to probe the peptide bonds of a set of 12 proteins with varied secondary structure contents. Their UVRR spectra show significant intensities for Phe and Tyr side chains, with small contributions from Trp side chains. They subtracted off the side chain contributions using UVRR spectra of the pure aromatic amino acids. The resulting corrected protein spectra were then used to compute pure secondary structure spectra of β -turn, α -helix, β -sheet and unordered structures via least-squares fitting. They illustrated the utility of their procedure by using the computed pure secondary structure spectra to determine the different secondary structural motifs in the temperature-dependent spectra of apomyoglobin. The computed pure secondary structure spectra enabled this determination.

JiJi and coworkers used the correlation optimized wraping (COW) method to remove the overlapping water bands in the AmI region of UVRR spectra.¹²⁶ They also used constrained multivariate curve resolution-alternating least squares (MCR-ALS) analysis¹²⁷ and parallel factor (PARAFAC) analysis¹²⁶ to resolve discrete protein secondary structural motifs.

Halsey et al. used UVRR spectroscopy to study membrane protein secondary structure and membrane-protein interactions.^{128,129} In their work, they measured multi-wavelength excited UVRR spectra of a lipid solubilized membrane protein, the *Rhodobacter capsulatus* cytochrome *bc*₁ complex (cyt bc₁). They observed that the AmI band intensity of cyt bc₁ increases dramatically compared to an aqueous soluble protein with similar secondary structure content. This was ascribed to dehydration of the backbone amides in the lipid. Deuterium exchange experiments confirmed that the spectral changes derived from the transmembrane α -helical portion of the protein complex.

UVRR spectroscopy was also used to gain insight into the structure of Barnase, a monomeric protein of 110 residues.¹³⁰ In their work, Couling, et al. used 244 nm excitation to excite Barnase in order to monitor Tyr band changes to probe changes in the protein structure that occurs upon folding into its native state. By using p-cresol as a reference, they calibrated the change in the intensity ratio of the Tyr doublet I₈₃₀/I₈₅₀ in terms of the Tyr HB strength, and obtained a linear relationship between the doublet relative intensity ratio and the HB enthalpies of formation.

UVRR was employed by Pieridou, et al. to determine the pKa of Tyr, as a peptide side chain and as the free amino acid.¹³¹ They used 239.5 nm excitation for the selective enhancement of the two Tyr residues in an 11-residue peptide fragment from transthyretin (TTR(105-115)) and monitored changes in Tyr Y8a band at different pHs. By monitoring the shifts in this band, they measured a titration curve which they fitted to a modified form of the Henderson-Hasselbach equation. They found that the pKa of the Tyr in the peptide (10.2) are slightly higher than that of aqueous Tyr monomer (9.1). They explained that the N-terminal Tyr 105 is easily exposed to solvent and its response to pH changes is similar to free Tyr. Tyr 114, on the other hand, may be involved in different HB interactions with neighbouring amino acid side chains and the peptide backbone. Thus, it is possible that these two Tyr residues sample two slightly different microenvironments in the peptide with the pKa of 10.2, representing an average value of the two Tyr.

4. UVRR STUDIES OF PROTEIN AND PEPTIDE FIBRILLATION

Protein fibrillation is often associated with human diseases such as Alzheimers, for example. The fact that numerous proteins and peptides fibrillize suggests that this conformation lies in the structural repertory of proteins, in general. The association of fibrillation with human disease motivates investigations of the structure of these fibers and their mechanism of formation.¹³² Unfortunately, the two classic tools of structural biology, X-ray crystallography and conventional NMR, are ill-suited for studying non-crystalline and insoluble full-length fibrils.¹³³ As shown below, deep UVRR is uniquely able to probe protein structure at all phases of fibrillation.¹³²⁻¹⁴² The use of chemometrics¹⁴³⁻¹⁵⁰ and two-dimensional correlation spectroscopy (2DCoS) to these UVRR studies dramatically increases the information content, as shown below.

4.1 Two-Dimensional Correlation Deep UV Resonance Raman Spectroscopy

Two-dimensional correlation spectroscopy (2DCoS) has recently found increasing use in vibrational spectroscopy.¹⁵¹ Vibrational 2DCoS is particularly beneficial for protein studies because it can resolve the often heavily overlapped bands in vibrational spectra into their separate components that arise from the various secondary structure motifs, amino acids and side-chain groups. Additionally, the sequential temporal information regarding conformational changes provided by 2DCoS enables determination of structural transitions and kinetic reaction mechanisms.¹³⁷

4.1.1 Fibril Nucleus Formation—Lednev's group demonstrated that deep UVRR combined with 2DCoS is a powerful tool for studying nucleus formation during fibrillation. Hen egg white lysozyme (HEWL), a protein chosen for its well-studied structural properties and folding/unfolding behaviors,¹³³ was used as a model for amyloidogenic proteins. Solutions of 70, 14, and 1.4 mg/mL of HEWL at pH 2.0 were incubated at 65 °C for various times. UVRR spectra were measured during incubation and the resulting kinetic spectral data were analyzed using 2DCoS.¹³⁶

Only random coil and β -sheet conformations are known to give rise to the C_{α} -H bending region intensities observed in the 1380–1400 cm⁻¹ region. Lednev et al. correlated C_{α} -H region band intensities with other UVRR bands.¹³⁷ Synchronous $\Phi(\nu_1, \nu_2)$ and asynchronous $\Psi(\nu_1, \nu_2)$ 2D-Raman spectra were calculated using Noda's approach:

$$\Phi(\nu_1, \nu_2) + i\Psi(\nu_1, \nu_2) = \frac{1}{\pi(T_{max} - T_{min})} \times \int_0^{\infty} \tilde{Y}_1(\omega) \tilde{Y}_2^*(\omega) d\omega \quad (3)$$

where $\tilde{Y}_1(\omega)$ and $\tilde{Y}_2^*(\omega)$ are the forward and conjugate Fourier transforms, respectively, of the experimental spectral intensities $\tilde{J}(\nu, t)$ for all frequencies ν from ν_1 to ν_2 and incubation times t , during the observation period from T_{min} to T_{max} .¹³⁶ In figure 18, only the C_{α} -H region and the α -helix sub-band of the Amide I region are shown for clarity.

The circled cross-peaks A, B, and C in figure 18, represent the peaks relating β -sheet to disordered structure, α -helix to β -sheet, and α -helix to disordered structure, respectively. Since the synchronous cross-peak A is positive and cross-peaks B and C are negative, β -sheet and disordered structure are positively correlated. Conversely, the negative peaks B and C imply negative correlations between α -helix and β -sheet, and α -helix and disordered structure. The asynchronous 2D-Raman correlation map (figure 18b) shows a positive peak at A, suggesting a change in the disordered structure spectral region happens first. Considering the negative synchronous peak, and the negative asynchronous peak at B, it can be deduced that spectral changes in the disordered structure spectral region happen before changes in the α -helix region. Similarly, the negative synchronous peak, and the positive

asynchronous peak at C implies that β -sheet spectral changes occur after α -helix changes.¹³⁷

4.1.2 Apparent Inverse Order—It is notable that at first glance, this interpretation of the 2D correlation maps suggests an anomalous sequence of events. Logically, α -helix melting needs to occur before any disordered structure can form. This apparent paradox is resolved by noting that the asynchronous 2DCoS probes both the sequential order of events in a chemical reaction and the average rate of concentration change of each species.¹³⁷ The latter is an important fact that, if overlooked, can lead to serious misinterpretation of spectroscopic data. This phenomenon can readily be explained by considering what contributes to an asynchronous 2D map. In any chemical reaction with the formation of an intermediate, the formation of the product will be in-phase with the decrease in the reactant, and thus, the intermediate should change slightly ahead to compensate for the delay in product formation.¹³⁷

4.1.3 Extraction of Characteristic Times for Structural Changes—The characteristic times for the evolution of secondary and tertiary structures were extracted from the 2D-UVRR data by means of $\kappa\nu$ correlation analysis. Following the approach of Shammukh et al.,¹⁵² the asynchronous correlation of the experimental decaying intensities with a reference set of exponentially decaying intensities was calculated by:

$$\Psi(\tau, \nu) = \frac{1}{N-1} \sum_{j=0}^{N-1} y(\nu, n_j) \sum_{k=0}^{N-1} N_{jk} \times \exp\left(\frac{-t}{\tau} + R\right) \quad (4)$$

where $\Psi(\tau, \nu)$ is the correlation intensity at a point (τ, ν) ; N is the total number of spectra; n_j is the order number of the spectrum; τ is the characteristic time of the exponential decay; N_{jk} is the Hilbert-Noda transformation matrix; R is the constant matrix, and $y(\nu, n)$ are the spectral intensities. After performing this analysis, the characteristic times were determined to be: disordered structure formation ($\tau \sim 22$ h), tertiary structure and α -helix melting ($\tau \sim 30$ h), and nucleus β -sheet formation ($\tau \sim 35$ h).¹³⁷

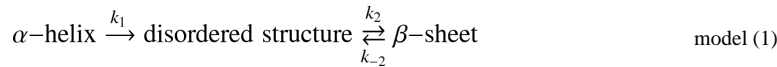
4.2 Elucidating the kinetic mechanism of early events of HEWL fibrillation

The asynchronous 2D-Raman correlation map suggests that the mechanism is stepwise, rather than parallel; otherwise, the formation of random coil and β -sheet would be completely correlated.¹³⁶ This implies that one of the four possible two-step mechanisms below is occurring. Table 1 summarizes the possible observations and corresponding interpretations of the 2D correlation data.

mechanism	(1)	$A \rightarrow B \rightarrow P$
mechanism	(2)	$A \iff B \rightarrow P$
mechanism	(3)	$A \rightarrow B \iff P$
mechanism	(4)	$A \iff B \iff P$

It has been shown that the formation of a partially unfolded intermediate from native HEWL is an irreversible transition.¹⁵³ This eliminates mechanisms (2) and (4) as possibilities. An irreversible conversion of B to P (mechanisms (1) and (2)) would appear in the 2D-Raman correlation map as a negative correlation between A and B at the beginning of the reaction, followed by a positive correlation between A and B for the remainder of the reaction. However, a reversible transition from B to P (mechanisms (3) and (4)) would lead to a negative correlation between A and B at all stages of the reaction, which was the case for

HEWL. Considering these details, only mechanism (3) remains, suggesting that the actual reaction mechanism is:



The rate constants k_1 , k_2 , and k_{-2} were determined by using the experimentally determined¹³⁶ characteristic times (summarized in table 2) for the mechanism:



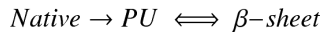
Relating the integrated rate laws for these two mechanisms yielded the following relations between the rate constants k_1 , k_2 , and k_{-2} and K_1 , K_2 , and K_{-2} :

$$\begin{aligned} k_1 &= K_1 \\ k_2 &= \frac{K_2}{1-R} \\ k_{-2} &= K_{-2} - \frac{R}{1-R} \times K_2 \end{aligned} \quad (5)$$

where R is the fraction of disordered structure in native HEWL (60%¹⁵⁴ in this case). Taking K_i to be the reciprocal of the characteristic time τ_{Ki} , one obtains $K_1 = 0.033 \text{ h}^{-1}$, $K_2 = 0.0125 \text{ h}^{-1}$, $K_{-2} = 0.067 \text{ h}^{-1}$, and thus, τ_{k1} , τ_{k2} , and τ_{k-2} are 30, 32, and 21 h, respectively.¹³⁷

A simulation-aided approach was utilized for model testing and the results proved to be in close agreement with experimental results. The rate constants k_1 , k_2 , and k_{-2} of model (1) were extracted by simulating different sets of rate constants k_i to calculate the evolution profiles of pure secondary structure. Using spectral profiles of the pure secondary structures, modeled as mixed Gaussian-Lorentzian shapes, and the simulated evolution profiles, kv correlation maps were constructed as described above, and compared to the experimental kv correlation maps. When the characteristic times were extracted from the best-matched kv correlation map, as described above, and converted to rate constants K_i , the results were identical to the experimentally derived rate constants.¹³⁷

These data are consistent with the step-by-step mechanism proposed by Dobson and coworkers:¹⁵⁵



Seeding experiments were performed to further test this interpretation. The supernatant of a HEWL sample that had been incubated for 48 hours was used to seed the fibrillation of fresh HEWL. The effective elimination of the fibrillation lag-phase observed is in complete agreement with the proposed mechanism.¹³⁶

4.3 Structural Characterization of Fibrillar Proteins

4.3.1 Hydrogen Deuterium Exchange—Lendev and coauthors have combined hydrogen-deuterium exchange (HX) with UVRR to probe the secondary structure of the fibril cross- β core. HX is such a useful technique for characterizing protein structure because in an amino acid residue, only the main chain NH group and O, N, and S bound protons can be exchanged easily, while the carbon-bound protons generally do not exchange.¹⁵⁶ This, combined with the fact that strongly hydrogen-bonded secondary structures greatly reduce the rate of hydrogen-deuterium exchange,¹⁵⁷ allows for a

particularly clever use of HX to probe the fibril core. It was hypothesized that the tightly packed hydrophobic core of amyloid fibrils would experience a drastically reduced HX rate compared to the amide N—H protons in the unordered fragments (Figure 19)¹⁴⁰. Mikhonin and Asher have shown⁸⁷ that HX will cause a down-shift of the amide II deep UVRR band from ~1555 to ~1450 cm⁻¹ (amide II') along with the virtual disappearance of the amide III band in an unordered protein.¹⁴² Figure 20 illustrates these spectral changes in deep UVRR spectra of fibrillar and unordered lysozyme upon deuteration.

4.3.2 Bayesian Source Separation—To deduce structural information about the fibril core, the overlapping spectral bands of the deuterated unordered fractions and the still-protonated cross- β core need to be resolved. The Bayesian approach¹⁵⁸ was utilized, instead of a blind source separation algorithm such as ICA or pure variable methods, because it is uniquely suited to solve extremely ill-suited MCR and prior-dominated problems.

4.3.3 Structure Determination of the Lysozyme Fibril Core—Lednev et al. combined deep UVRR spectroscopy and hydrogen-deuteron exchange to probe the structure of HEWL fibrils.¹⁴² The Bayesian signal dictionary approach was used to incorporate *a priori* information about characteristic spectral bands. In this work, the reference band library contained mixed Gaussian and Lorentzian shapes of certain widths and spectral positions obtained by fitting the deep UVRR spectra of fibrils with Gaussian/Lorentzian peaks having a pre-defined width range. Prior information regarding the experimental spectra of deuterated lysozyme and reference spectrum for the cross- β -sheet were incorporated by augmenting the matrices with an additional row. The final step is accomplished by using the floating point genetic algorithm to determine the remaining parameters.¹⁴⁰

By extracting the deep UVRR spectrum of the fibril core, the exact position of the amide III₃(β) band could be determined, and Asher group's method was used to calculate of the Ψ dihedral angle distribution.¹⁴² The spectrum of the cross- β -core of HEWL fibrils extracted by this method is shown in figure 21. The distribution of the Ψ dihedral angle obtained from the Raman signature of the fibril core provides an important characteristic of the polypeptide conformation and should allow for differentiating different types of cross- β core in amyloid fibrils.

4.3.4 Structural Variations in the Cross- β Core

4.3.4.1 YEHK Genetically Engineered Polypeptides: Over 20 structurally and functionally unrelated proteins that are associated with various neurodegenerative diseases form similar fibrillar assemblies despite the fact that the fibrillation conditions and the apparent mechanism of fibrillation are protein specific. Lednev and coworkers utilized relatively simple polypeptides to mimic the fibril formation of globular proteins. Several synthetic polypeptides exhibiting typical fibrillogenic properties have been designed and synthesized by using genetic engineering.¹⁵⁹⁻¹⁶² These large polypeptides are soluble under close to physiological conditions, but form fibrils under acidic pH. They exhibit a lag phase and show accelerated fibrillation on seeding or agitation. Genetic engineering allows for varying the polypeptide sequence to probe the sequence specific mechanism of fibrillation.

A large 687-residue polypeptide consisting 32 amino acid repeats, GH₆[(GA)₃GY(GA)₃GE(GA)₃GH(GA)₃GK]₂₁GAH₆ (YEHK21) was found to form fibrils at room temperature.¹⁶³ The formation of these fibrils was thermoreversible. Deep UVRR spectra were recorded at various temperatures ranging from 25 to 90 °C, after reaching equilibrium. The most significant spectral changes occurred at temperatures greater than 80 °C. Figure 22 shows the Raman spectra of YEHK21 in solution measured at 25 and 90 °C.

The spectra demonstrate changes consistent with the melting of a β -sheet structure into an unordered conformation. Spectra measured at various times after heating were virtually the same, indicating a slow recovery process.¹⁶³

The analysis of polypeptide secondary structure content was complicated by the temperature dependence of the basis spectra. This was overcome by exploiting the slow recovery process. Deep UVRR spectra were recorded after 5 minutes of heating to various temperatures ranging from 25 to 125°C, and subsequent rapid cooling to room temperature. In this way, all measurements were taken at the same temperature, ensuring any spectral changes were a result of temperature-induced conformational changes (Figure 23). This spectral dataset was used for understanding YEHK21 polypeptide melting.¹⁶³

A melting curve was constructed using a basis set of three deep UVRR spectra: the YEHK21 backbone Raman spectra (initial sample and sample treated at 125°C) and the deep UVRR spectrum of tyrosine. The first two spectra represent completely folded YEHK21 (mostly β -sheet and turn conformation), and the unordered YEHK21 (mainly polyproline II conformation), while tyrosine was included for use as an internal standard. These three basis spectra were used to fit the Raman spectra of YEHK21 at various temperatures; figure 23 shows the calculated and residual spectra for the samples treated at 35 and 85 °C. This showed that the melting process could be considered as a two-state process with each spectrum described with different proportions of β -sheet and turn/ polyproline II conformations. The percent of folded contribution was plotted versus temperature to create the melting curve of figure 24.¹⁶³

Thermodynamic parameters were estimated by fitting the data to:

$$f_F = \frac{1}{1 + e^{-(\frac{\Delta H}{RT} - \frac{\Delta S}{R})}} \quad (6)$$

where f_F is the fraction of folded polypeptide after treatment at temperature T and R is the gas constant. The parameters ΔH and ΔS were determined to be 135 ± 14 kJ/mol and 370 ± 40 J/(mol K), where the standard error was represented by $\pm 2\sigma$. This represents a first approximation because equation (6) is typically applied to two-state processes where ΔC_p , the heat capacity change, has negligible effect on the enthalpy of folding over the narrow temperature range of the transition.¹⁶⁴

Temperature jump experiments were performed to analyze the kinetics of YEHK21 β -sheet melting. The deep UVRR spectra of YEHK21 were collected every 20 seconds after a temperature jump from 25 to 85°C (figure 25a). The results of the temperature jump experiments were similar to the steady-state measurements; the spectrum in figure 25d is quite similar to those shown in figure 25b,c,e,f. It was also found that recovery of the YEHK21 Raman spectrum was dependent on the temperature to which it was heated before being cooled to room temperature. Complete recovery of the YEHK21 Raman spectrum was observed after approximately 6 hours of standing at room temperature after being briefly heated to 85 °C. On the other hand, only 80% recovery was achieved after a 5-minute heating to 100 °C before sitting at room temperature for 4 hours. The kinetics for the recovery of the deep UVRR spectrum after heating was determined to be roughly monoexponential with a characteristic time of approximately 1 hour.¹⁶³

A study of three similarly engineered polypeptides that form amyloid-like fibrils provided the first direct evidence that the structure of the cross- β core is sequence-dependent. The three polypeptides consisted of seven repeats of 32, 40, or 48 amino acid repeats, $(GA)_nGY(GA)_nGE(GA)_nGH(GA)_nGK$ ($n = 3, 4$, or 5 , respectively, 32YEHK7, 40YEHK7,

or 48YEHK7). These β -sheet-forming repetitive polypeptide blocks and selected amino acids at turn positions facilitated the formation of the targeted amyloid-like fibrils¹⁴¹ (Figure 26A). These polypeptides were designed to have the same turn structure so any pair-wise subtraction would result in the pure resonance Raman spectra of the fibrillar β -sheet core.¹⁴⁰ The validity of this hypothesis is verified by inspecting the difference spectrum in figure 26C, where they are virtually identical within experimental error.¹⁴¹

The studies above are the first direct measurements of the β -turn spectroscopic signature. Pure variable methods¹⁶⁵ (see Supporting Information) were used to analyze the spectra of the YEHK fibrils to resolve the contributions from the β -sheet and β -turn portions. The spectra of the two components were calculated and the experimental spectra of the YEHK fibrils were able to be fit with a linear combination of the two components (Figure 27). Using the Raman signature of the cross- β core, the dominant amide III peak was found to be 1241 cm⁻¹, corresponding to a Ψ angle of 150° and an antiparallel β -sheet conformation. The narrow Ramachandran Ψ angular distribution of YEHK fibrils suggests a highly ordered β -sheet,¹⁴¹ consistent with the findings reported on lysozyme fibrils.¹⁴² Notably, however, the UVRR spectra of the cross- β core of YEHK and lysozyme were different, indicating a sequence dependence of the core β -structure.¹⁴¹

4.3.4.2 Amyloid β : The application of the HX-DUVRR method to Amyloid β (A β) fibrils revealed that parallel and antiparallel β -sheets have different distributions of Ψ dihedral angles. Full-length unlabeled A β ₁₋₄₀ peptide and A β ₃₂₋₄₂ fragment fibrils were subjected to post fibrillation HX, UVRR spectra of the fibrillar core extracted, and the Ψ dihedral angle distributions calculated. It was shown that A β ₁₋₄₀ peptide exhibited a parallel β -sheet conformation, atypical for globular proteins, and that A β ₃₂₋₄₂ fragment fibrils possessed the more typical antiparallel conformation.¹³⁵ The availability of the 3-dimensional structure of the A β ₁₋₄₀ fibrils obtained by solid-state NMR¹⁶⁶ was used to verify the applicability of the Asher group's approach⁸² for the quantitative characterization of peptide conformation in the fibril core using DUVRR spectroscopy.

Using this structural information, the amide III region of the deep UVRR spectra of the A β ₁₋₄₀ fibril core was calculated by using the following method, and compared to experimental results. The contributions of each peptide residue in the β -strand that was resistant to HX were calculated using a set of residue-specific Ψ angles reported for the A β ₁₋₄₀ fibril core¹⁶⁶ as Gaussian curves with a half-width at half-maximum of 13 cm⁻¹. As shown in figure 28b, the calculated spectrum (blue) is in excellent agreement with the experimental spectrum (black). It is notable that there is a significant difference in the spectral profile of the A β ₁₋₄₀ fibril core (Figure 28b), and those of the A β ₃₂₋₄₂ (Figure 30a), hamster prion protein and YEHK peptide (Figure 28c). The major difference between the calculated amide III band region and the experimentally measured one is the appearance of two bands at 1280 and 1250 cm⁻¹. These bands, however, are also present in the spectrum of A β ₃₂₋₄₂, and are outside the β -sheet region; indicating that these peaks are most likely not part of the amide III₃ vibration and do not interfere with the analysis.

4.3.5 Aromatic Side Chain as a Reporter of Local Environment—Xu et al.¹³³ assessed phenylalanine's ability to act as an intrinsic deep UVRR spectroscopic probe of local environment. A 1.17 mM *N*-acetyl-L-phenylalanine ethyl ester (ac-phe-ee) solution in acetonitrile was diluted in a series of acetonitrile-water solutions with a final acetonitrile content ranging from 5% to 100% and deep UVRR spectra were recorded. As seen in figure 29, the spectra were comprised of two strong peaks corresponding to acetonitrile, and several prominent phenylalanine bands. The band at 1000 cm⁻¹, derives from phenyl ring stretching, exhibited the strongest change in Raman cross section as the concentration of acetonitrile varied. The inset of figure 29 shows that the Raman cross section of this band

increases monotonically, reaching a plateau at approximately 50% acetonitrile. Practically, this indicates that the 1000 cm^{-1} band of phenylalanine is sensitive to water exposure, making it a probe of protein local environment and tertiary structure.

In the study of HEWL, deep UVRR spectra were recorded at various stages of fibrillation, analyzing the supernatant and gelatinous phase separately (Figure 30). The spectra were dominated by contributions of the amide chromophore and phenylalanine. There was a dramatic reduction in the 1000 cm^{-1} phenylalanine band intensity with increased incubation time. Figure 31 shows the monoexponential decrease with a characteristic time of $29 \pm 2\text{ h}$. This indicates that phenylalanine is increasingly exposed to water as fibrillation progresses.¹³⁷

JiJi and coworkers also used deep UVRR spectroscopy to study amyloid- β ($A\beta$) peptide fibrillation.¹⁶⁷ They observed that the intensities of phe and tyr bands increase upon addition of myricetin which inhibits $A\beta$ peptide fibrillation. They concluded that myricetin interacts with these aromatic amino acid side chains and prohibits fibrillation of $A\beta$ peptide.

4.4 Spontaneous Refolding of Amyloid Fibrils from One Polymorph to Another

Amyloid fibrils prepared from full-length proteins are typically very stable and considered to be the most thermodynamically stable form of proteins because of the high resistance to thermal and solvent-induced denaturation.^{168,169} Very harsh denaturing conditions such as high pH, low temperature and high pressure are required to disintegrate mature fibrils,^{170,171} and no newly formed fibrils are expected to appear under such conditions. The ability of mature fibrils to change their structure and morphology has not been questioned, to the best of our knowledge, because no conventional methods would allow its detection without special sample preparation.

Kurouski et al.¹⁷² utilized deep UVRR spectroscopy to monitor the stability of apo- α -lactalbumin fibrils during the preparation of samples for atomic force microscopic (AFM) characterization. UVRR spectroscopy was chosen since it does not require any sample preparation. Surprisingly, melting and refolding of β -sheet was evident in the Raman spectra measured for mature apo- α -lactalbumin fibrils after the temperature was dropped from 37°C to 25°C and the solution was desalted (Figure 32).

Later, deep UVRR spectroscopy was also used to characterize the initial (Polymorph I) and final (Polymorph II) polymorphs.¹⁷² The hydrogen-deuterium exchange combined with deep UVRR spectroscopy (see above for details) indicated that the amide III₃ region of the Polymorph I spectrum shows two strong peaks at 1226 and 1253 cm^{-1} , corresponding to Ψ dihedral angles of 134.5 and 163.5° . Polymorph II, however, only exhibited a peak at 1253 cm^{-1} suggesting only a single β -sheet form is present, clearly indicating a difference in the structure of the fibril cores.¹³⁴ This result showed that changes in the fibril cross- β core correlate with noticeable changes in fibril morphology, indicating that apo- α -lactalbumin fibril polymorphism is correlated by a specific organization of the fibril core. The application of deep UVRR spectroscopy provided a unique opportunity for detecting the spontaneous transition between the two fibril polymorphs, observations that were not easily evident by using other conventional biophysical methods.¹⁷²

5. CONCLUSIONS

UVRR is a powerful tool for the study of biomolecular structure and dynamics. The field is at present small due to the costs of instrumentation and the lack of commercial instruments. The instrumentation will continue to advance due to improvements in laser technology and the development of UV Raman spectrometers with dramatically improved signal-to-noise

ratio (SNR) that will enable secondary structure conformational analysis at the level of single peptide bonds in large proteins.

With sufficient SNR, the Gibbs free energy landscape of individual peptide bonds in a peptide or protein can be incisively measured by selective isotopic labeling of individual peptide bonds. The difference spectrum between the labeled and the natural abundance protein would reveal the AmIII₃ band of each peptide bond; the frequencies and bandshapes will reveal the distribution in Ψ angles for each peptide bond. The resulting Gibbs free energy landscape for each isotopically substituted peptide bond will specify the individual peptide bond energy landscape. T-jump kinetic measurements can probe the activation barriers that control (un)folding mechanisms.

Deep UVRR is uniquely suitable for structural characterization of proteins at all stages of amyloid fibril formation. The combination of hydrogen-deuterium exchange with DUVRR spectroscopy allows for probing the variations in cross- β core structure of fibril polymorphs. The application of advanced statistics, chemometrics and two-dimensional correlation spectroscopy in particular, for DUVRR spectra analysis significantly increases the quality and amount of information on protein structure and dynamics. This approach is especially useful for establishing the kinetic mechanisms of amyloid fibrillation.

Supplementary Material

Refer to Web version on PubMed Central for supplementary material.

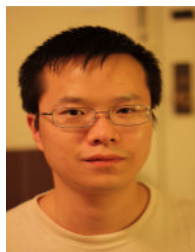
Acknowledgments

The authors gratefully acknowledge NIH Grants # 1R01EB009089 and R01AG033719 for funding.

Biography



Sulayman Oladepo received his PhD from the University of Alberta in 2010, under the supervision of Prof. Glen Loppnow. He spent a year as a postdoctoral associate in the laboratory of Prof. Sanford Asher at the University of Pittsburgh where he used UV resonance Raman spectroscopy to study the melting dynamics of β -sheet structures and the effects of citrullination on protein folding dynamics. He is currently a visiting fellow at Canmet Energy Technology Centre, Devon, Alberta. His current research involves photoacoustic FTIR and Raman spectroscopic characterization of asphaltenes.



Kan Xiong received his Bachelor's Degree in Chemistry from the University of Science and Technology of China in 2006. He is currently a senior graduate student under the direction

of Prof. Sanford A. Asher at the University of Pittsburgh and is working on using Raman spectroscopy to study protein folding and $\text{Cl}^- \rightarrow \text{H}_2\text{O}$ charge transfer.



Zhenmin Hong is currently a graduate student in the Department of Chemistry, University of Pittsburgh. He received B.S. and M.S. degrees from Tsinghua University, China. His research interest includes using UV resonance Raman spectroscopy to study protein and peptide structure and folding. He is now examining the effect of side chain interactions on determining peptide conformations.



Sanford Asher is Distinguished Professor of Chemistry at the University of Pittsburgh. He received his Bachelor's degree from the University of Missouri at St. Louis in 1971 and his PhD in 1977 from UC Berkeley. Following a postdoctoral work in Applied Physics at Harvard, he joined the department of Chemistry of the University of Pittsburgh in 1980. His current research concentrates on developing UV resonance Raman spectroscopy for probing protein structure and dynamics. His research group also investigates and develops photonic crystal materials and sensors.



Joseph Handen received his Bachelor's Degree in Chemistry from the University at Albany, State University of New York in 2009. He is currently a graduate student in Dr. Igor Lednev's research group at the University at Albany, State University of New York and is working on using Raman spectroscopy to study β -sheet structures in amyloidogenic polypeptides.



Igor K. Lednev is an associate professor at the University at Albany, State University of New York. He graduated from the Moscow Institute of Physics and Technology, Russian Federation, receiving his Ph.D. degree in 1983. Then Dr. Lednev worked at the Institute of Chemical Physics, Russian Academy of Sciences, as a group leader. He joined the University at Albany in 2002. Dr. Lednev's research is focused on the development and application of novel laser spectroscopy for biomedical research and forensic purposes.

REFERENCES

1. Baldwin RL, Rose GD. Trends Biochem. Sci. 1999; 24:26. [PubMed: 10087919]
2. Baldwin RL, Rose GD. Trends Biochem. Sci. 1999; 24:77. [PubMed: 10098403]
3. Dobson CM. Phil. Trans. R. Soc. Lond. B. 2001; 356:133. [PubMed: 11260793]
4. Dobson CM, Sali A, Karplus M. Angew. Chem. Int. Ed. 1998; 37:868.
5. Jahn TR, Radford SE. FEBS J. 2005; 272:5962. [PubMed: 16302961]
6. Lindberg MO, Oliveberg M. Curr. Opin. Struct. Biol. 2007; 17:21. [PubMed: 17251003]
7. Daggett V, Fersht A. Nat. Rev. Mol. Cell Biol. 2003; 4:497. [PubMed: 12778129]
8. Anfinsen CB, Haber E, Sela M, White FH Jr. Proc. Natl. Acad. Sci. U. S. A. 1961; 47:1309. [PubMed: 13683522]
9. Matthews CR. Ann. Rev. Biochem. 1993; 62:653. [PubMed: 8352599]
10. Thirumalai D, Woodson SA. Acc. Chem. Res. 1996; 29:433.
11. Kim PS, Baldwin RL. Ann. Rev. Biochem. 1982; 51:459. [PubMed: 6287919]
12. Karplus M, Weaver DL. Nature. 1976; 260:404. [PubMed: 1256583]
13. Baldwin RL. Trends Biochem. Sci. 1989; 14:291. [PubMed: 2672452]
14. Daggett V, Fersht AR. Trends Biochem. Sci. 2003; 28:18. [PubMed: 12517448]
15. Dill KA, Ozkan SB, Shell MS, Weikl TR. Annu. Rev. Biophys. 2008; 37:289. [PubMed: 18573083]
16. Dill KA, Chan HS. Nat. Struct. Biol. 1997; 4:10. [PubMed: 8989315]
17. Dill KA. Protein Sci. 1999; 8:1166. [PubMed: 10386867]
18. Zhuravlev PI, Papoian GA. Q. Rev. Biophys. 2010; 43:295. [PubMed: 20819242]
19. Kim J, Keyes T, Straub JE. Phys. Rev. E: Stat., Nonlinear, Soft Matter Phys. 2009; 79:030902.
20. Rylance GJ, Johnston RL, Matsunaga Y, Li CB, Baba A, Komatsuzaki T. Proc. Natl. Acad. Sci. U. S. A. 2006; 103:18551. [PubMed: 17132739]
21. Angelani L, Ruocco G. EPL. 2009; 87:18002.
22. Zhuravlev PI, Papoian GA. Curr. Opin. Struct. Biol. 2010; 20:16. [PubMed: 20102791]
23. Oliveira LC, Schug A, Onuchic JN. J. Phys. Chem. B. 2008; 112:6131. [PubMed: 18251535]
24. Gruebele M. Proc. Natl. Acad. Sci. U. S. A. 2009; 106:18879. [PubMed: 19889984]
25. Mello CC, Barrick D. Proc. Natl. Acad. Sci. U. S. A. 2004; 101:14102. [PubMed: 15377792]
26. Levy Y, Jortner J, Becker OM. Proc. Natl. Acad. Sci. U. S. A. 2001; 98:2188. [PubMed: 11226214]
27. Karplus M, McCammon JA. Nat. Struct. Biol. 2002; 9:646. [PubMed: 12198485]
28. Noé F, Schütte C, Vandenh-Eijnden E, Reich L, Weikl TR. Proc. Natl. Acad. Sci. U. S. A. 2009; 106:19011. [PubMed: 19887634]
29. Freddolino PL, Harrison CB, Liu Y, Schulten K. Nat. Phys. 2010; 6:751. [PubMed: 21297873]
30. Cantor, CR.; Schimmel, PR. *Biophysical Chemistry*. McCombs, LW., editor. Vol. 2. W. H. Freeman and Company; San Francisco: 1980. p. 402
31. Rosenheck KD,P. Proc. Natl. Acad. Sci. U. S. A. 1961; 47:1775. [PubMed: 14494018]
32. Saxena VP, Wetlaufer DB. Proc. Natl. Acad. Sci. U S A. 1971; 68:969. [PubMed: 5280530]
33. Greenfield NJ, Fasman GD. Biochemistry. 1969; 8:4108. [PubMed: 5346390]
34. Dickerson RE. Annu. Rev. Biochem. 1972; 41:815. [PubMed: 4117310]
35. Strandberg B, Dickerson RE, Rossmann MG. J. Mol. Biol. 2009; 392:2. [PubMed: 19712775]

36. Moffat K. *Acta Crystallogr. Sect. A*. 1998; 54:833. [PubMed: 9859195]
37. Mittermaier A, Kay LE. *Science*. 2006; 312:224. [PubMed: 16614210]
38. Billeter M. Q. *Rev. Biophys.* 1992; 25:325. [PubMed: 1470680]
39. Wuthrich K. *Acta Crystallogr. Sect. D-Biol. Crystallogr.* 1995; 51:249. [PubMed: 15299291]
40. Frank AT, Stelzer AC, Al-Hashimi HM, Andricioaei I. *Nucleic Acids Res.* 2009; 37:3670. [PubMed: 19369218]
41. Andronesi OC, Becker S, Seidel K, Heise H, Young HS, Baldus M. *J. Am. Chem. Soc.* 2005; 127:12965. [PubMed: 16159291]
42. Williams S, Causgrove TP, Gilmanish R, Fang KS, Callender RH, Woodruff WH, Dyer RB. *Biochemistry*. 1996; 35:691. [PubMed: 8547249]
43. Hendra, PJ. *Handbook of vibrational spectroscopy*. Chalmers, JP.; Griffiths, PR., editors. Vol. 2. John Wiley & Sons; London: 2002.
44. Everall, N. *Handbook of vibrational spectroscopy*. Chalmers, JP.; Griffiths, PR., editors. Vol. 1. John Wiley & Sons; London: 2002.
45. Weber, A. *Handbook of vibrational spectroscopy*. Chalmers, JP.; Griffiths, PR., editors. Vol. 1. John Wiley & Sons; London: 2002.
46. Long, DA. *THE RAMAN EFFECT: a unified treatment of the theory of raman scattering by molecules*. West Sussex; England: 2002.
47. Kramers H, Heisenberg W. *Z. Phys. A: Hadrons Nucl.* 1925; 31:681.
48. Dirac PAM. *Proc. R. Soc. London, Ser. A*. 1927; 114:710.
49. Placzek, G. *Handbuch der Radiologie*. Marx, E., editor. Vol. 6. Aeademische; Leipzig: 1934.
50. Albrecht AC. *J. Chem. Phys.* 1961; 34:1476.
51. Lee S-Y, Heller EJ. *J. Chem. Phys.* 1979; 71:4777.
52. Tannor DJ, Heller EJ. *J. Chem. Phys.* 1982; 77:202.
53. Heller EJ, Sundberg R, Tannor D. *J. Phys. Chem.* 1982; 86:1822.
54. Asher SA. *Ann. Rev. Phys. Chem.* 1988; 39:537. [PubMed: 3075468]
55. Myers AB. *J. Raman Spectrosc.* 1997; 28:389.
56. Asher SA. *Anal. Chem.* 1993; 65:A59.
57. Asher SA. *Anal. Chem.* 1993; 65:A201.
58. Palaniappan V, Bocian DF. *Biochemistry*. 1994; 33:14264. [PubMed: 7947837]
59. Chi ZH, Asher SA. *Biochemistry*. 1998; 37:2865. [PubMed: 9485437]
60. Balakrishnan G, Hu Y, Oyerinde OF, Su JT, Spiro TG. *J. Am. Chem. Soc.* 2007; 294:504. [PubMed: 17227009]
61. Ray GB, Copeland RA, Lee CP, Spiro TG. *Biochemistry*. 1990; 29:3208. [PubMed: 2159329]
62. Ahmed Z, Beta IA, Mikhonin AV, Asher SA. *J. Am. Chem. Soc.* 2005; 127:10943. [PubMed: 16076200]
63. Asher S, Johnson C. *Science*. 1984; 225:311. [PubMed: 6740313]
64. Terner JS, J. D, Spiro TG, Nagumo M, Nicol M, El-Sayed MA. *Proc. Natl. Acad. Sci. U. S. A.* 1981; 78:1313. [PubMed: 16592986]
65. Smulevich G, Spiro TG. *Biochimica et Biophysica Acta*. 1985; 830:80.
66. Asher SA, Johnson CR, Murtaugh J. *Rev. Sci. Instrum.* 1983; 54:1657.
67. Bykov S, Lednev I, Ianoul A, Mikhonin A, Munro C, Asher SA. *Appl. Spectrosc.* 2005; 59:1541. [PubMed: 16390595]
68. Lednev IK, Ermolenkov VV, He W, Xu M. *Anal. Bioanal. Chem.* 2005; 381:431. [PubMed: 15625596]
69. Balakrishnan G, Hu Y, Spiro TG. *Appl. Spectrosc.* 2006; 60:347. [PubMed: 16613628]
70. Asher SA, Bormett RW, Chen XG, Lemmon DH, Cho N, Peterson P, Arrigoni M, Spinelli L, Cannon J. *Appl. Spectrosc.* 1993; 47:628.
71. Sparrow MC, Jackovitz JF, Munro CH, Hug WF, Asher SA. *Appl. Spectrosc.* 2001; 55:66.
72. Holtz JSW, Bormett RW, Chi ZH, Cho NJ, Chen XG, Pajcini V, Asher SA, Spinelli L, Owen P, Arrigoni M. *Appl. Spectrosc.* 1996; 50:1459.

73. Zhao XJ, Chen RP, Tengroth C, Spiro TG. *Appl. Spectrosc.* 1999; 53:1200.
74. Huang CY, Balakrishnan G, Spiro TG. *J. Raman Spectrosc.* 2006; 37:277.
75. Ahmed Z, Scaffidi JP, Asher SA. *Biopolymers.* 2009; 91:52. [PubMed: 18932268]
76. Kallenbach, NR.; Lyu, P.; Zhou, H. Circular dichroism and conformational analysis of biomolecules. Fasman, GD., editor. Plenum Press; New York: 1996. p. 201
77. Sharma B, Bykov SV, Asher SA. *J. Phys. Chem. B.* 2008; 112:11762. [PubMed: 18712913]
78. Asher SA, Chi ZH, Li PS. *J. Raman Spectrosc.* 1998; 29:927.
79. Chen XG, Asher SA, Schweitzerstennner R, Mirkin NG, Krimm S. *J. Am. Chem. Soc.* 1995; 117:2884.
80. Myshakina NS, Asher SA. *J. Phys. Chem. B.* 2007; 111:4271. [PubMed: 17394301]
81. Bykov SV, Asher SA. *J. Phys. Chem. Lett.* 2010; 1:269. [PubMed: 20657703]
82. Mikhonin AV, Bykov SV, Myshakina NS, Asher SA. *J. Phys. Chem. B.* 2006; 110:1928. [PubMed: 16471764]
83. Mikhonin AV, Ahmed Z, Ianoul A, Asher SA. *J. Phys. Chem. B.* 2004; 108:19020.
84. Lednev IK, Karnoup AS, Sparrow MC, Asher SA. *J. Am. Chem. Soc.* 1999; 121:8074.
85. Wang Y, Purrello R, jordan T, Spiro TG. *J. Am. Chem. Soc.* 1991; 113:6359.
86. Mix G, Schweitzer-Stenner R, Asher SA. *J. Am. Chem. Soc.* 2000; 122:9028.
87. Mikhonin AV, Asher SA. *J. Phys. Chem. B.* 2005; 109:3047. [PubMed: 16851319]
88. Chi ZH, Chen XG, Holtz JSW, Asher SA. *Biochemistry.* 1998; 37:2854. [PubMed: 9485436]
89. Sharma B, Asher SA. *J. Phys. Chem. B.* 2010; 114:6661. [PubMed: 20420366]
90. Chen XG, Li PS, Holtz JSW, Chi ZH, Pajcini V, Asher SA, Kelly LA. *J. Am. Chem. Soc.* 1996; 118:9705.
91. Asher SA, Ianoul A, Mix G, Boyden MN, Karnoup A, Diem M, Schweitzer-Stenner R. *J. Am. Chem. Soc.* 2001; 123:11775. [PubMed: 11716734]
92. Myshakina NS, Ahmed Z, Asher SA. *J. Phys. Chem. B.* 2008; 112:11873. [PubMed: 18754632]
93. Oboodi MR, Alva C, Diem M. *J. Phys. Chem.* 1984; 88:501.
94. Ianoul A, Boyden MN, Asher SA. *J. Am. Chem. Soc.* 2001; 123:7433. [PubMed: 11472179]
95. Asher SA, Mikhonin AV, Bykov S. *J. Am. Chem. Soc.* 2004; 126:8433. [PubMed: 15238000]
96. Shi Z, Olson C, Rose G, Baldwin R, Kallenbach N. *Proc. Natl. Acad. Sci. U S A.* 2002; 99:9190. [PubMed: 12091708]
97. Mikhonin AV, Myshakina NS, Bykov SV, Asher SA. *J. Am. Chem. Soc.* 2005; 127:7712. [PubMed: 15913361]
98. Krimm S, Mark JE. *Proc. Natl. Acad. Sci. U. S. A.* 1968; 60:1122. [PubMed: 16591670]
99. Ma L, Ahmed Z, Mikhonin AV, Asher SA. *J. Phys. Chem. B.* 2007; 111:7675. [PubMed: 17567063]
100. Lednev IK, Karnoup AS, Sparrow MC, Asher SA. *J. Am. Chem. Soc.* 2001; 123:2388. [PubMed: 11456888]
101. Lednev IK, Karnoup AS, Sparrow MC, Asher SA. *J. Am. Chem. Soc.* 1999; 121:4076.
102. Munoz V, Thompson PA, Hofrichter J, Eaton WA. *Nature.* 1997; 390:196. [PubMed: 9367160]
103. JiJi RD, Balakrishnan G, Hu Y, Spiro TG. *Biochemistry.* 2006; 45:34. [PubMed: 16388578]
104. Huang CY, Balakrishnan G, Spiro TG. *Biochemistry.* 2005; 44:15734. [PubMed: 16313176]
105. Balakrishnan G, Hu Y, Bender GM, Getahun Z, DeGrado WF, Spiro TG. *J. Am. Chem. Soc.* 2007; 129:12801. [PubMed: 17910449]
106. Balakrishnan G, Hu Y, Case MA, Spiro TG. *J. Phys. Chem. B.* 2006; 110:19877. [PubMed: 17020373]
107. Mikhonin A, Asher S, Bykov S, Murza A. *J. Phys. Chem. B.* 2007; 111:3280. [PubMed: 17388440]
108. Balakrishnan G, Hu Y, Bender GM, Getahun Z, DeGrado WF, Spiro TG. *Biophys. J.* 2005; 88:39A.
109. Balakrishnan G, Hu Y, Case MA, McLendon GA, Spiro TG. *Biophys. J.* 2004; 86:499A. [PubMed: 14695294]

110. Ianoul A, Mikhonin A, Lednev IK, Asher SA. *J. Phys. Chem. A.* 2002; 106:3621.
111. Mikhonin A, Asher S. *J. Am. Chem. Soc.* 2006; 128:13789. [PubMed: 17044707]
112. Phillips CM, Mizutani Y, Hochstrasser RM. *Proc. Natl. Acad. Sci. U. S. A.* 1995; 92:7292. [PubMed: 7638183]
113. Lian T, Locke B, Kholodenko Y, Hochstrasser M. *J. Phys. Chem.* 1994; 98:11648.
114. Hashimoto S, Fukasaka J, Takeuchi H. *J. Raman Spectrosc.* 2001; 32:557.
115. Chi ZH, Asher SA. *Biochemistry.* 1999; 38:8196. [PubMed: 10387065]
116. Hughson FM, Wright PE, Baldwin RL. *Science.* 1990; 249:1544. [PubMed: 2218495]
117. Haruta N, Kitagawa T. *Biochemistry.* 2002; 41:6595. [PubMed: 12022863]
118. Sato A, Mizutani Y. *Biochemistry.* 2005; 44:14709. [PubMed: 16274218]
119. Sanchez KM, Neary TJ, Kim JE. *J. Phys. Chem. B.* 2008; 112:9507. [PubMed: 18588328]
120. El-Mashtoly SF, Yamauchi S, Kumauchi M, Hamada N, Tokunaga F, Unno M. *J. Phys. Chem. B.* 2005; 109:23666. [PubMed: 16375346]
121. Kim JE, Pan DH, Mathies RA. *Biochemistry.* 2003; 42:5169. [PubMed: 12731857]
122. Kaminaka S, Mathies RA. *Laser Chem.* 1999; 19:165.
123. Chen J, Barry BA. *Photochemistry and Photobiology.* 2008; 84:815. [PubMed: 18282183]
124. Chen J, Bender SL, Keough JM, Barry BA. *J. Phys. Chem. B.* 2009; 113:11367. [PubMed: 19639977]
125. Okishio N, Fukuda R, Nagai M, Nagai Y, Nagatomo S, Kitagawa T. *J. Raman Spectrosc.* 1998; 29:31.
126. Simpson JV, Oshokoya O, Wagner N, Liu J, JiJi RD. *Analyst.* 2011; 136:1239. [PubMed: 21267503]
127. Simpson JV, Balakrishnan G, JiJi RD. *Analyst.* 2009; 134:138. [PubMed: 19082186]
128. Halsey CM, Oshokoya OO, JiJi RD, Cooley JW. *Biochemistry.* 2011; 50:6531. [PubMed: 21718040]
129. Halsey CM, Xiong J, Oshokoya OO, Johnson JA, Shinde S, Beatty JT, Ghirlanda G, JiJi RD, Cooley JW. *ChemBioChem.* 2011; 12:2125. [PubMed: 21796753]
130. Couling VW, Foster NW, Klenerman D. *J. Raman Spectrosc.* 1997; 28:33.
131. Pieridou GK, Hayes SC. *Phys. Chem. Chem. Phys.* 2009; 11:5302. [PubMed: 19551197]
132. Lednev IK, Shashilov V, Xu M. *Curr. Sci.* 2009; 97:180.
133. Xu M, Ermolenkov VV, Uversky VN, Lednev IK. *J. Biophotonics.* 2008; 1:215. [PubMed: 19412971]
134. Lednev, I.; Kurouski, D.; Lauro, W. Amyloid Fibrils are “Alive” as Evident from Deep UV Raman Spectroscopic Examination: an Instrumentation Driven Approach. 2010. p. 172
135. Popova LA, Kodali R, Wetzel R, Lednev IK. *J. Am. Chem. Soc.* 2010; 132:6324. [PubMed: 20405832]
136. Shashilov V, Xu M, Ermolenkov VV, Fredriksen L, Lednev IK. *J. Am. Chem. Soc.* 2007; 129:6972. [PubMed: 17500518]
137. Shashilov VA, Lednev IK. *J. Am. Chem. Soc.* 2008; 130:309. [PubMed: 18067295]
138. Shashilov VA, Lednev IK. *J. Raman Spectrosc.* 2009; 40:1749.
139. Shashilov VA, Lednev IK. *Chem. Rev.* 2010; 110:5692. [PubMed: 20593900]
140. Shashilov VA, Sikirzhytski V, Popova LA, Lednev IK. *Methods.* 2010; 52:23. [PubMed: 20580825]
141. Sikirzhytski V, Topilina NI, Higashiya S, Welch JT, Lednev IK. *J. Am. Chem. Soc.* 2008; 130:5852. [PubMed: 18410104]
142. Xu M, Shashilov V, Lednev IK. *J. Am. Chem. Soc.* 2007; 129:11002. [PubMed: 17705492]
143. Brereton, RG. *Chemometrics: Data Analysis for the Laboratory and Chemical Plant.* Wiley; Chichester, England: 2003. p. 489
144. Hyvarinen, A.; Karhunen, J.; Oja, E. *Independent Component Analysis.* John Wiley & Sons Inc.; 2002. p. 145-164.
145. Hyvarinen A, Hoyer PO, Inki M. *Neural Comput.* 2001; 13:1527. [PubMed: 11440596]

146. Shao XG, Wang GQ, Wang SF, Su QD. *Anal. Chem.* 2004; 76:5143. [PubMed: 15373454]
147. Cichocki, A.; Amari, SI. *Adaptive Blind Signal and Image Processing: Lerning Algorithms and Applications*. John Wiley; Chichester, New York: 2002. p. 554
148. Cichocki, A.; Amari, SI. *Adaptive Blind Signal and Image Processing: Lerning Algorithms and Applications*. John Wiley; Chichester, New York: 2002. p. 554
149. Bell AJ, Sejnowski TJ. *Neural Comput.* 1995; 7:1129. [PubMed: 7584893]
150. Hyvarinen A, Oja E. *Neural Networks*. 2000; 13:411. [PubMed: 10946390]
151. Noda, I.; Ozaki, Y. *Two-Dimensional Correlation Spectroscopy: Applications in Vibrational and Optical Spectroscopy*. John Wiley & Sons; Chichester, West Sussex, England; Hoboken, NJ: 2004.
152. Shanmukh S, Dluhy RA. *J. Phys. Chem. A*. 2004; 108:5625.
153. Xu M, Shashilov VA, Ermolenkov VV, Fredriksen L, Zagorevski D, Lednev IK. *Protein Sci.* 2007; 16:815. [PubMed: 17400924]
154. Artymiuk PJ, Blake CCF, Rice DW, Wilson KS. *Acta Crystallogr. Sect. B-Struct. Sci.* 1982; 38:778.
155. Booth DR, Sunde M, Bellotti V, Robinson CV, Hutchinson WL, Fraser PE, Hawkins PN, Dobson CM, Radford SE, Blake CCF, Pepys MB. *Nature*. 1997; 385:787. [PubMed: 9039909]
156. Englander SW, Sosnick TR, Englander JJ, Mayne L. *Curr. Opin. Struct. Biol.* 1996; 6:18. [PubMed: 8696968]
157. DeFlores LP, Tokmakoff A. *J. Am. Chem. Soc.* 2006; 128:16520. [PubMed: 17177399]
158. Knuth KH. *SPIE*. 1998; 3459:147.
159. Topilina NI, Ermolenkov VV, Higashiya S, Welch JT, Lednev IK. *Biopolymers*. 2007; 86:261. [PubMed: 17377970]
160. Topilina NI, Ermolenkov VV, Sikirzytski V, Higashiya S, Lednev IK, Welch JT. *Biopolymers*. 2010; 93:607. [PubMed: 20162724]
161. Topilina NI, Higashiya S, Rana N, Ermolenkov VV, Kossow C, Carlsen A, Ngo SC, Wells CC, Eisenbraun ET, Dunn KA, Lednev IK, Geer RE, Kaloyeros AE, Welch JT. *Biomacromolecules*. 2006; 7:1104. [PubMed: 16602727]
162. Topilina NI, Sikirzytsky V, Higashiya S, Ermolenkov VV, Lednev IK, Welch JT. *Biomacromolecules*. 2010; 11:1721. [PubMed: 20553038]
163. Lednev IK, Ermolenkov VV, Higashiya S, Popova LA, Topilina NI, Welch JT. *Biophys. J.* 2006; 91:3805. [PubMed: 16891363]
164. Swint L, Robertson AD. *Protein Sci.* 1993; 2:2037. [PubMed: 8298454]
165. Windig W, Gallagher NB, Shaver JM, Wise BM. *Chemometrics and Intelligent Laboratory Systems*. 2005; 77:85.
166. Petkova AT, Ishii Y, Balbach JJ, Antzutkin ON, Leapman RD, Delaglio F, Tycko R. *Proc. Natl. Acad. Sci. U. S. A.* 2002; 99:16742. [PubMed: 12481027]
167. Wang M, Ji Ji RD. *J. Biophotonics*. 2011; 4:637. [PubMed: 21702084]
168. Baskakov, IV. *Amyloid Proteins: The Beta Sheet Conformation and Disease*. Sipe, JD., editor. WILEY-VCH; Weinheim: 2005.
169. Wolf MG, Gestel J, de Leeuw SW. *Methods Mol. Biol.* 2008; 474:153. [PubMed: 19031066]
170. Brange J, Andersen L, Laursen ED, Meyn G, Rasmussen E. *J. Pharm. Sci.* 1997; 86:517. [PubMed: 9145374]
171. Kim HY, Cho MK, Riedel D, Fernandez CO, Zweckstetter M. *Angew. Chem. Int. Ed.* 2008; 47:5046.
172. Kurouski D, Lauro W, Lednev IK. *Chem. Comm.* 2010; 46:4249. [PubMed: 20532285]

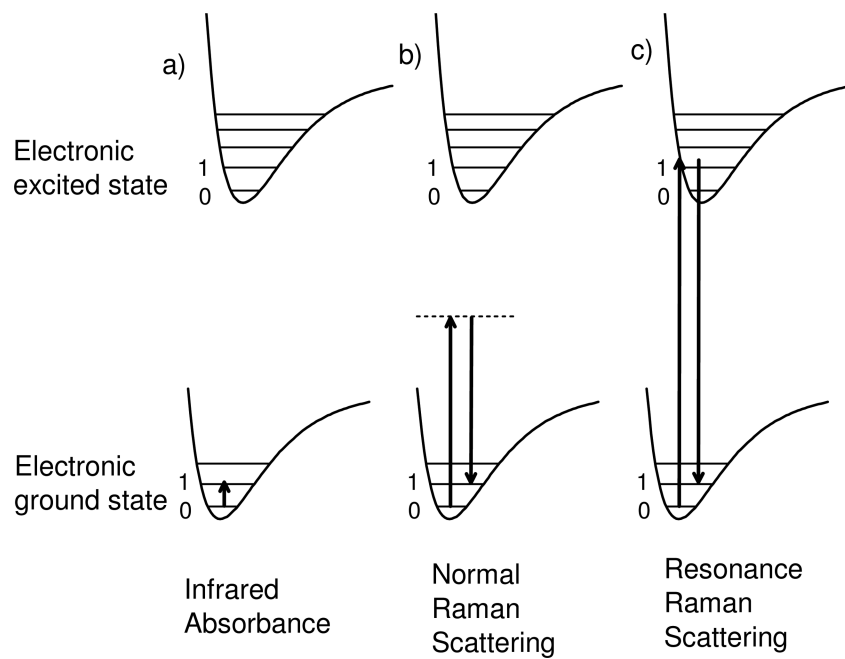
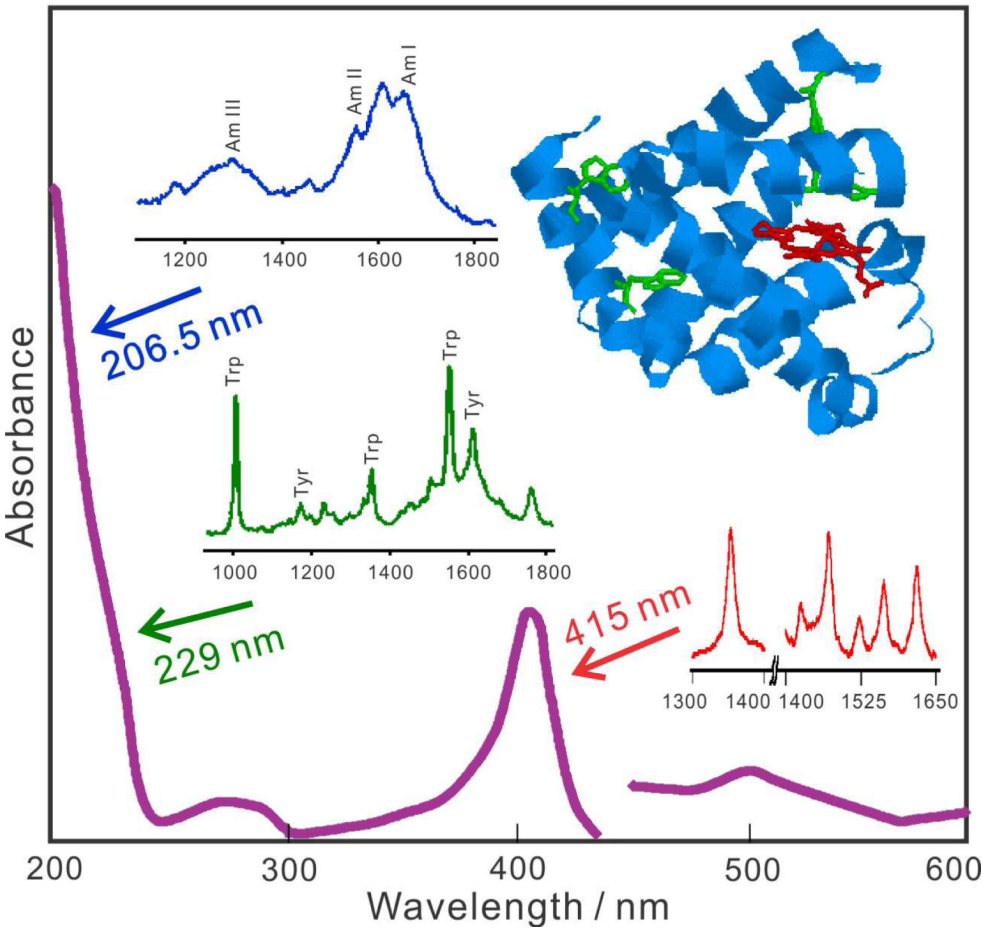


Figure 1.

Comparison of infrared absorption, normal Raman scattering and resonance Raman scattering.

**Figure 2.**

Selectivity of resonance Raman spectral measurements of myoglobin showing the protein absorption spectrum and the different resonance Raman spectra obtained with different excitation wavelengths.

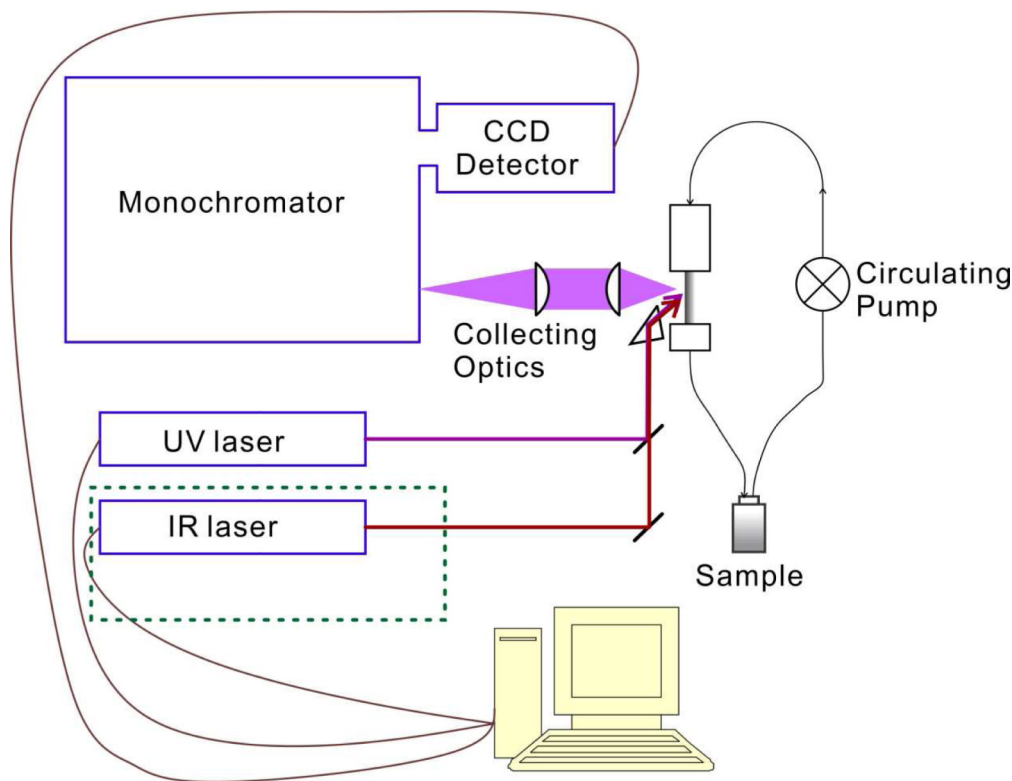


Figure 3.

Schematic diagram of a typical back scattering UVRR instrument, which utilizes an IR laser to achieve T-jump kinetic measurements.

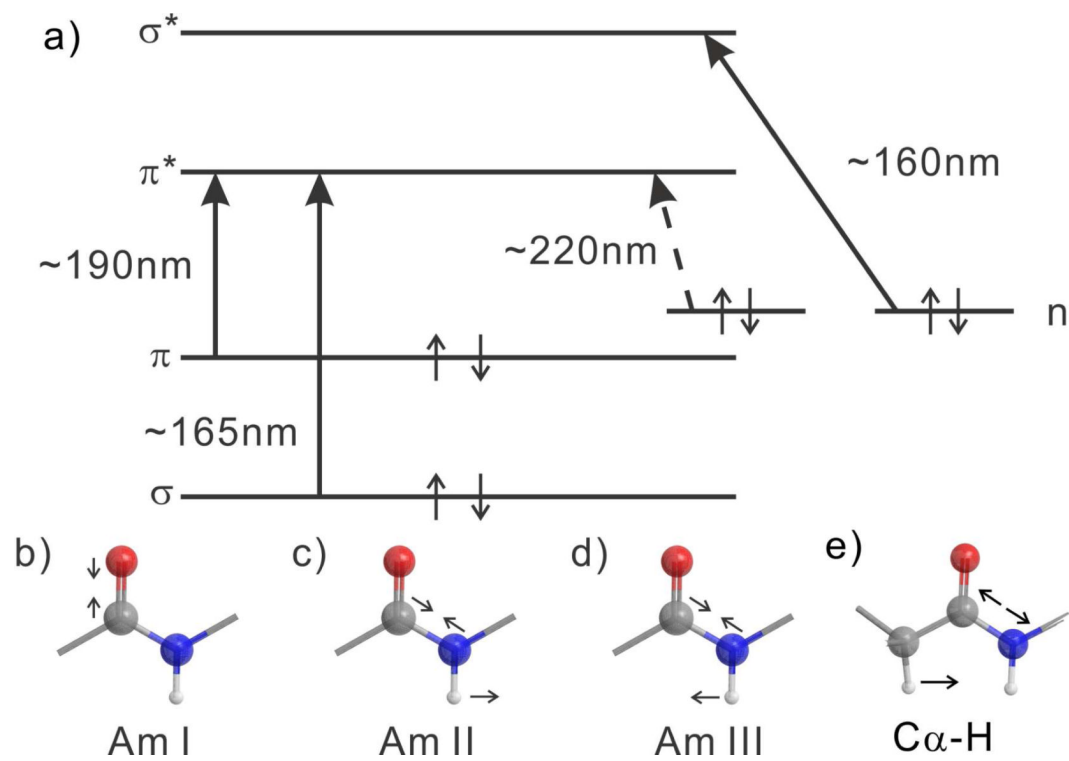


Figure 4.

a) HOMO and LUMO orbitals of peptide bonds in peptides and proteins and b)-e) UVRR enhanced peptide bond vibrational modes.

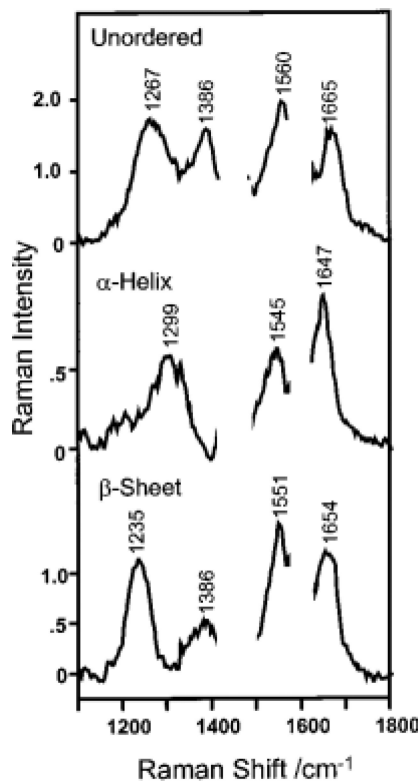


Figure 5.

Pure secondary structure UVRR basis spectra obtained from a library of protein UVRR spectra. The regions around 1610 and 1450 cm^{-1} are excluded because their spectral conformational dependence is not completely understood. Adapted with permission from Reference 88. Copyright 1998 American Chemical Society.

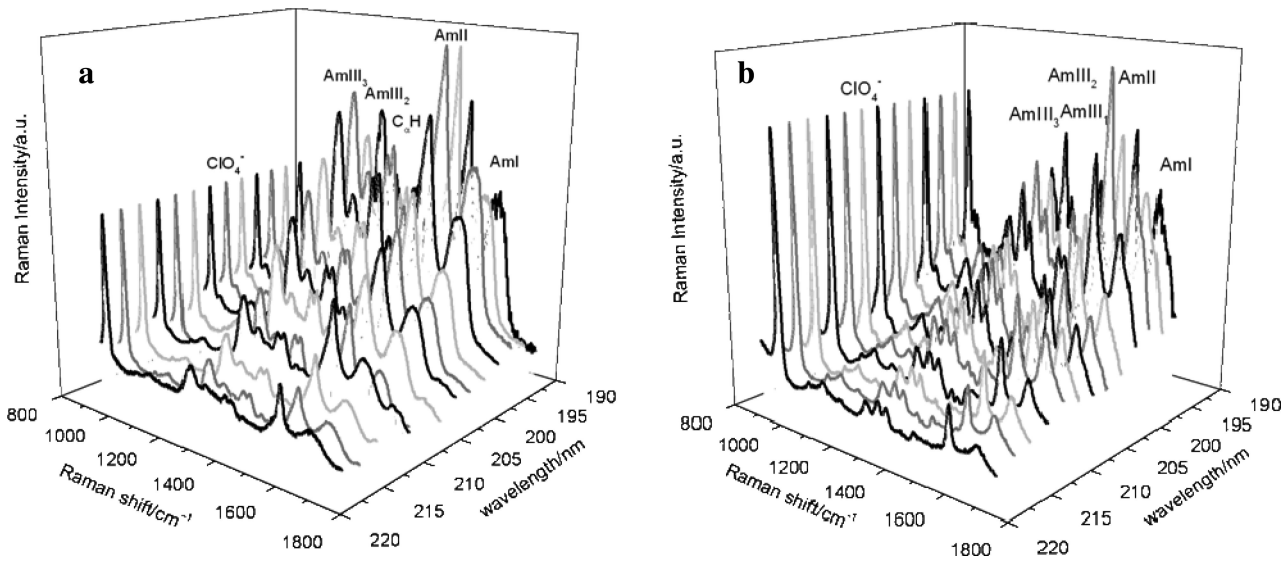


Figure 6.

(a) Observed UVRR spectra between 218 and 194 nm of AP in a PPII-like conformation at 60 °C. (b) UVRR spectra between 218 and 194 nm of α -helix conformation of AP at 5 °C obtained by subtracting the appropriate amount of PPII UVRR spectrum at each excitation wavelength. Both sets of spectra show similar but not identical enhancement patterns. All spectra were normalized to the $932 \text{ cm}^{-1} \text{ ClO}_4^-$ internal standard. Adapted with permission from Reference 77. Copyright 2008 American Chemical Society.

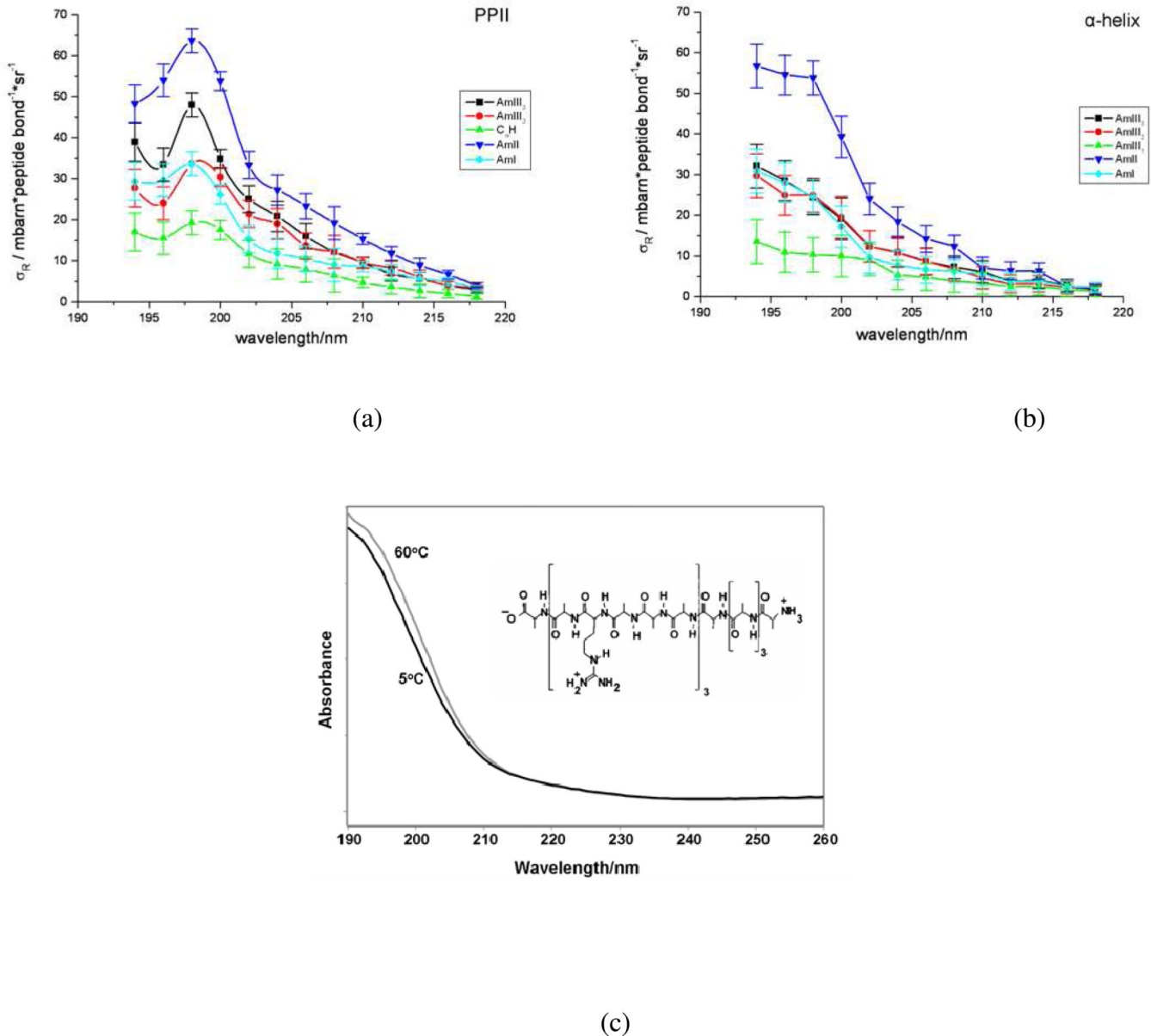


Figure 7.
Absolute Raman cross sections excitation profiles between 194 to 218 nm for (a) PPII-like conformation and (b) α -helix conformations of AP. (c) UV-vis absorption spectrum of AP at 5 °C, where it is predominantly α -helical, and at 60 °C, where it is in a predominantly PPII-like conformation. Inset: Structure of AP. Adapted with permission from Reference 77. Copyright 2008 American Chemical Society.

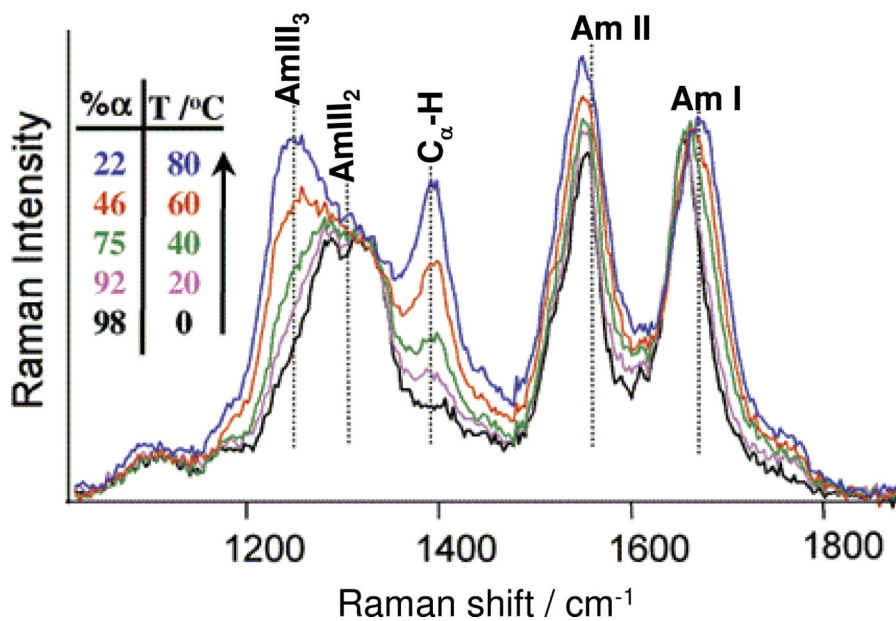


Figure 8.

The temperature dependence of the UVRR spectra and resulting α -helix fractions of poly-L-glutamic acid at pH 4.3 calculated from the UVRR spectra. Adapted with permission from Reference 91. Copyright 2001 American Chemical Society.

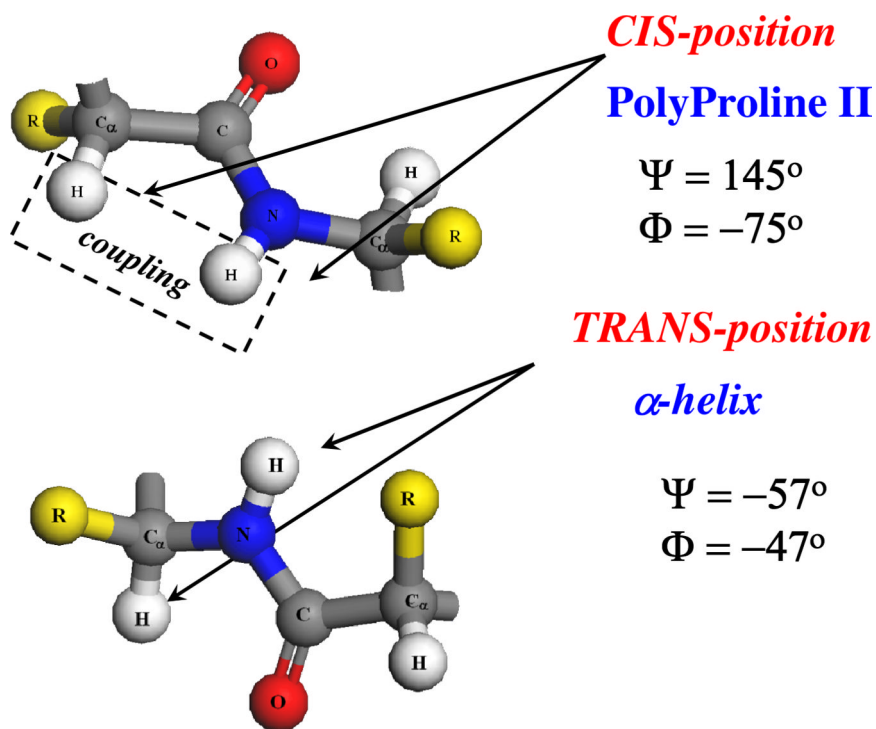
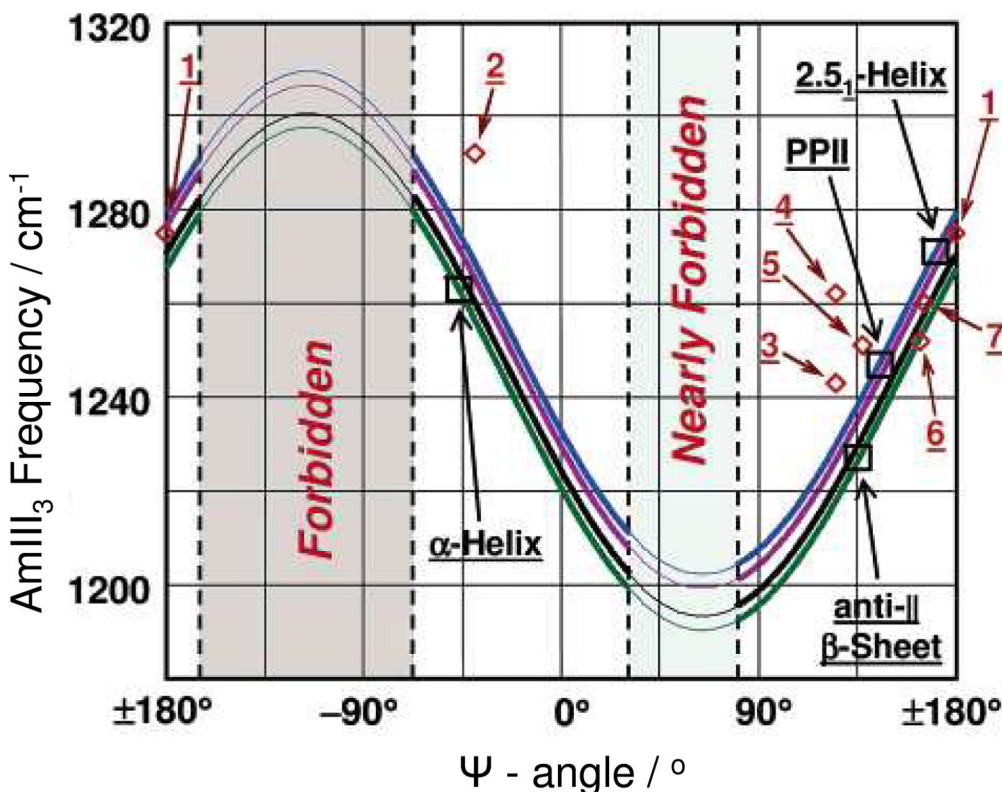


Figure 9.
Relative orientations of N-H and C_α-H bonds in the polyproline II and α -helix conformations.

**Figure 10.**

Correlation between AmIII_3 frequency, peptide bond HB pattern and Ramachandran Ψ angle: (□) measured AmIII_3 frequencies of α -helix, antiparallel β -sheet, PPII and 2.5_1 -helix in aqueous solution; (\diamond) measured AmIII_3 frequencies of peptide crystals, plotted against their Ψ angles: 1 Ala-Asp, 2 Gly-Ala-Leu· $3\text{H}_2\text{O}$, 3 Val-Glu, 4 Ala-Ser, 5 Val-Lys, 6 Ser-Ala, 7 Ala-Ala. Blue curve is the predicted correlation (eq. 1) for full HB to water (PPII, 2.5_1 -helix, and extended β -strand); green curve is a theoretically predicted correlation (eq. 1) for two end-on peptide bond-peptide bond HBs (α -helix-like conformation, and interior strands of β -sheet); magenta curve is the predicted correlation (eq. 1) for peptide bond where only the C=O group has a peptide bond-peptide bond HB (three α -helix N-terminal peptide bonds, and half of peptide bonds of the exterior strands of β -sheet); black curve is the predicted correlation (eq. 1) for peptide bond with just their N-H group peptide bond involved in a peptide bond-peptide bond HB (three α -helix C-terminal peptide bonds, and half that of peptide bond of exterior strand of β -sheet). Adapted with permission from Reference 82. Copyright 2006 American Chemical Society.

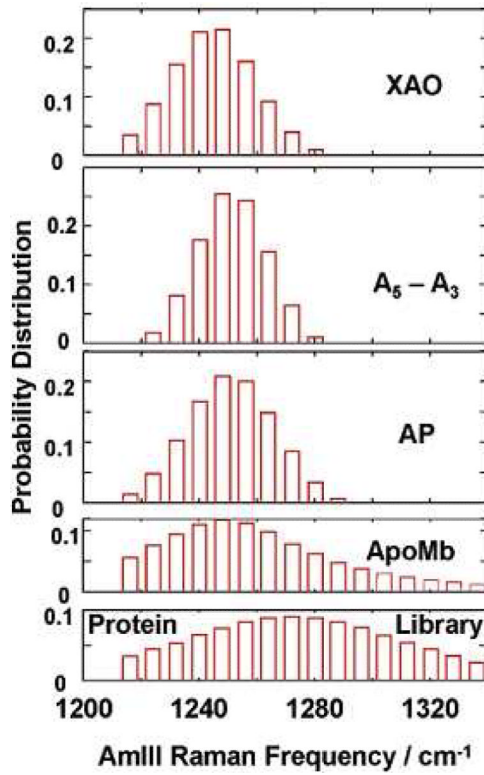


Figure 11.

Frequency distribution of AmIII₃ band calculated by deconvolution of homogenously broadened AmIII₃ band profiles of XAO of the sequence Ac-XXAAAAAAOO-NH₂ (A is alanine, O is ornithine, X is diaminobutyric acid), A₅-A₃ (ala₅-ala₃), non- α -helical AP of the sequence AAAAA-(AAARA)₃A, acid-denatured apomyoglobin, and the frequency distribution of spectra of a library of proteins. The resulting histogram shows the population distribution underlying the measured AmIII₃ bands. Adapted with permission from Reference 95. Copyright 2004 American Chemical Society.

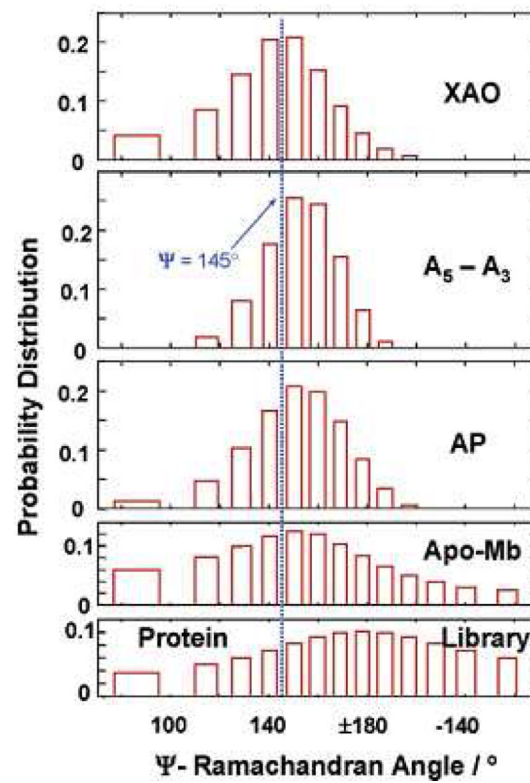
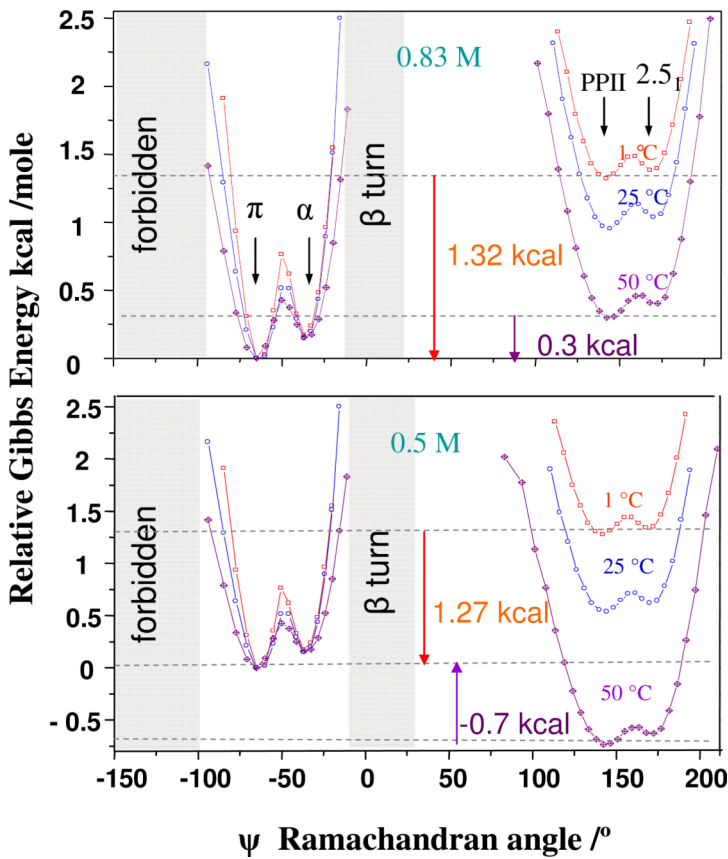


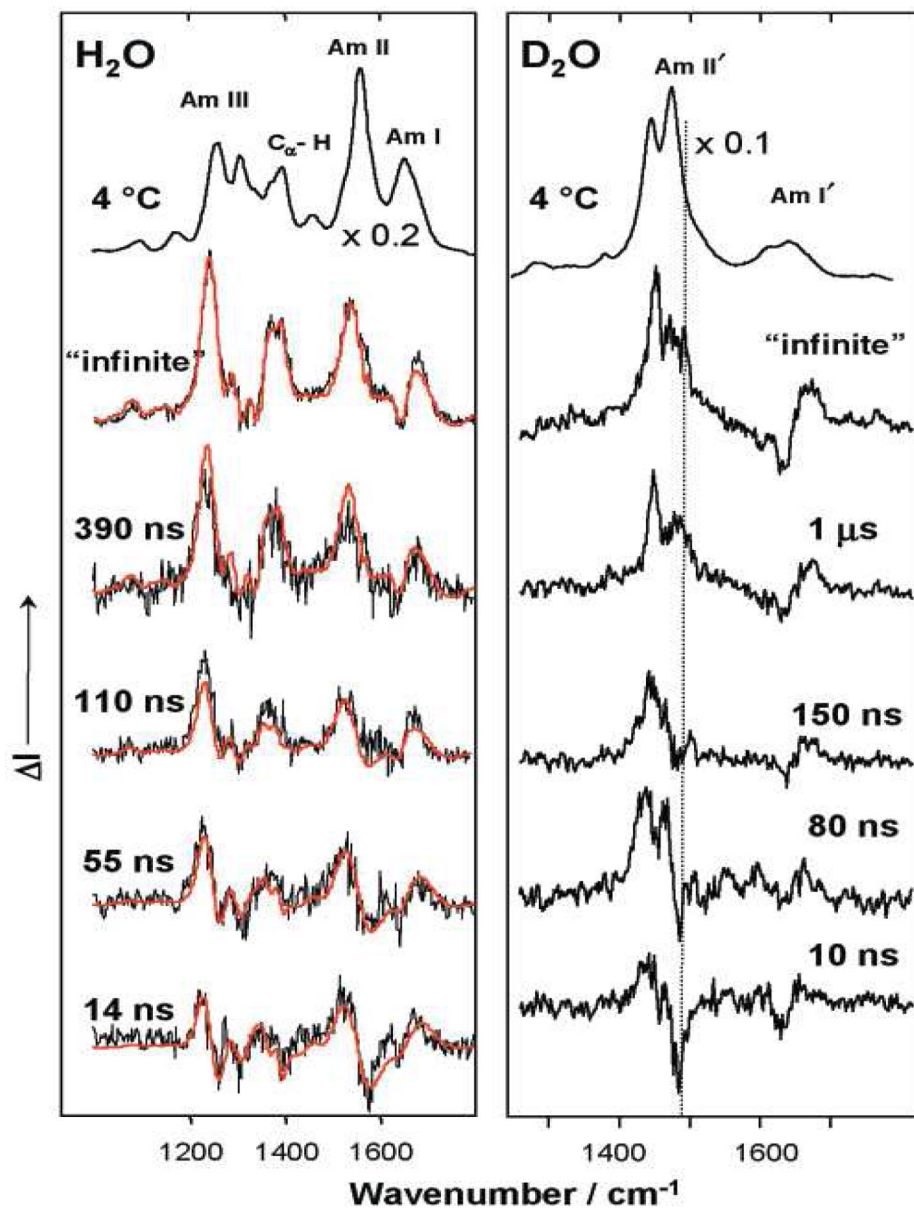
Figure 12.

Estimated Ramachandran Ψ angle distribution of XAO, $A_5 - A_3$, non- α -helical AP, acid-denatured apomyoglobin, and “disordered” protein conformations. Adapted with permission from Reference 95. Copyright 2004 American Chemical Society.

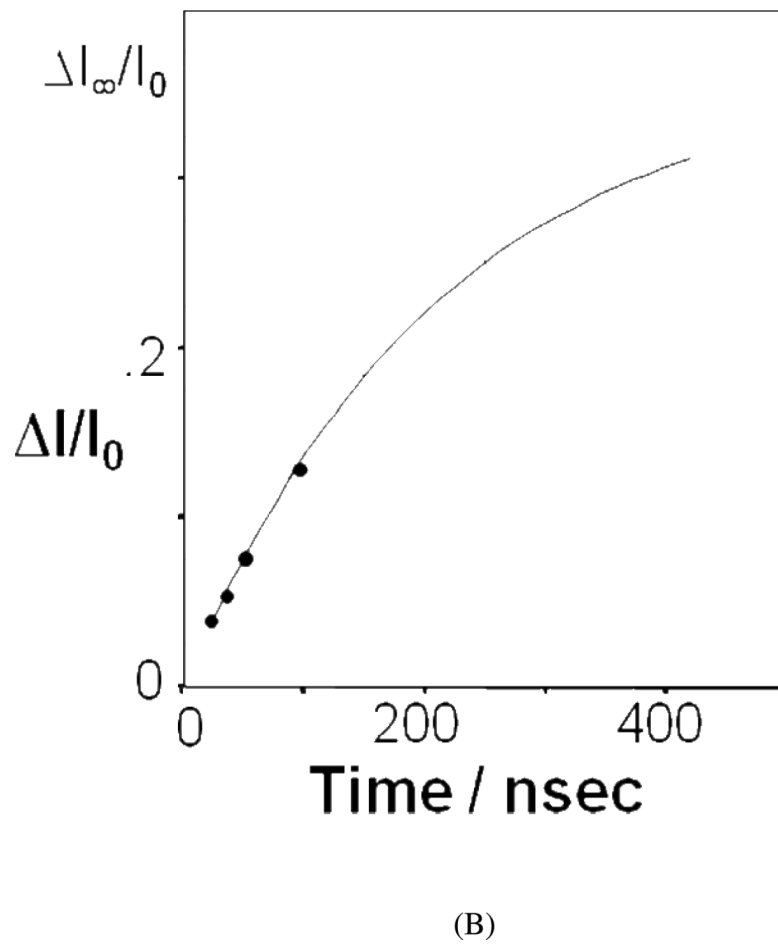
**Figure 13.**

Estimated Gibbs free energy landscape for poly-L-lysine in 0.83 and 0.5 M NaClO₄ at 1 °C, 25 °C and 50 °C. Increasing the NaClO₄ concentration from 0.5 M to 0.83 M stabilizes α -helix-like conformations. Higher temperatures stabilize the unfolded conformations.

Adapted with permission from Reference 99. Copyright 2007 American Chemical Society.



(A)



(B)

Figure 14.

(A) AP UVRR spectra measured in water and D₂O solution at 4°C (top), and transient difference spectra of AP in solution initially at 4 °C measured at different delay times following a T-jump of ~31 °C (~22 °C in D₂O). (B) Kinetics of thermal denaturation of AP. The ordinate axis is the relative change in the UV Raman intensity at 1236 cm⁻¹ obtained from transient difference spectra of Fig. 14 of ref. 84. The abscissa is the time delay at which the spectra were acquired following the T-jump. (A) Adapted with permission from Reference 100. Copyright 2001 American Chemical Society. (B) Adapted with permission from Reference 84. Copyright 1999 American Chemical Society.

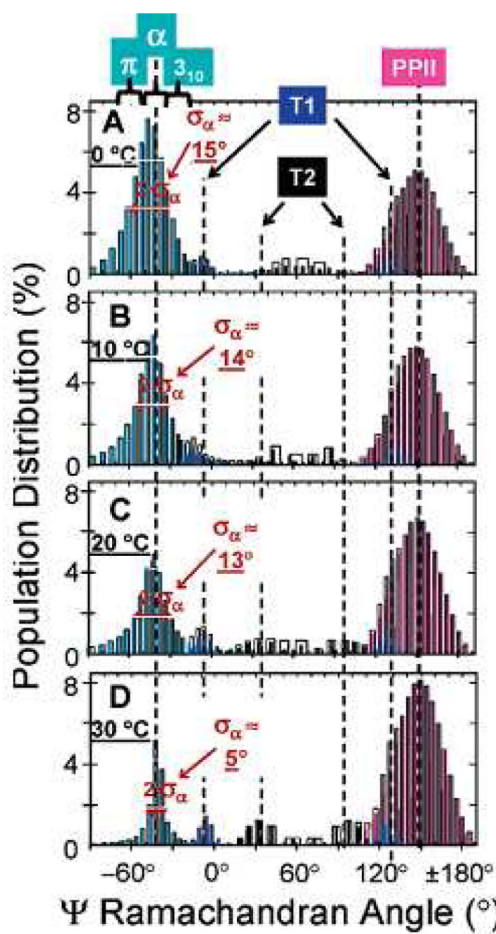
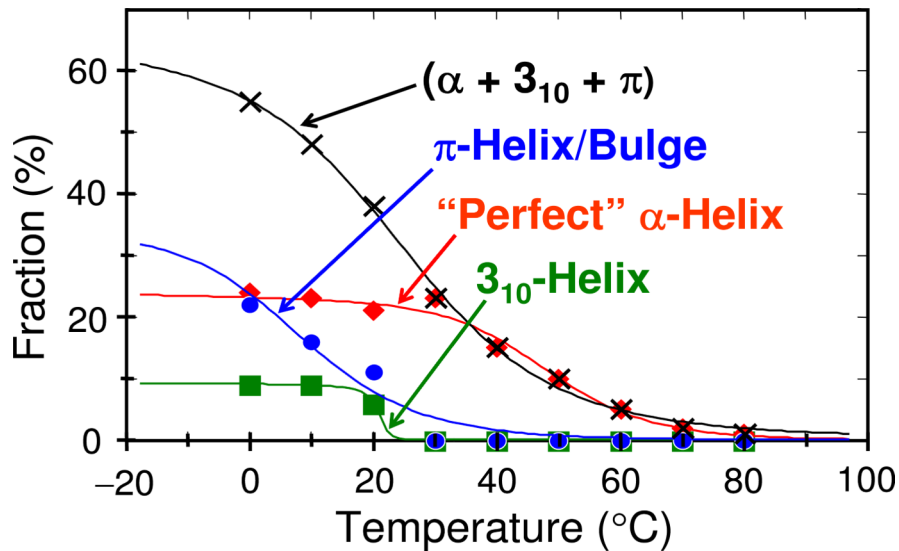
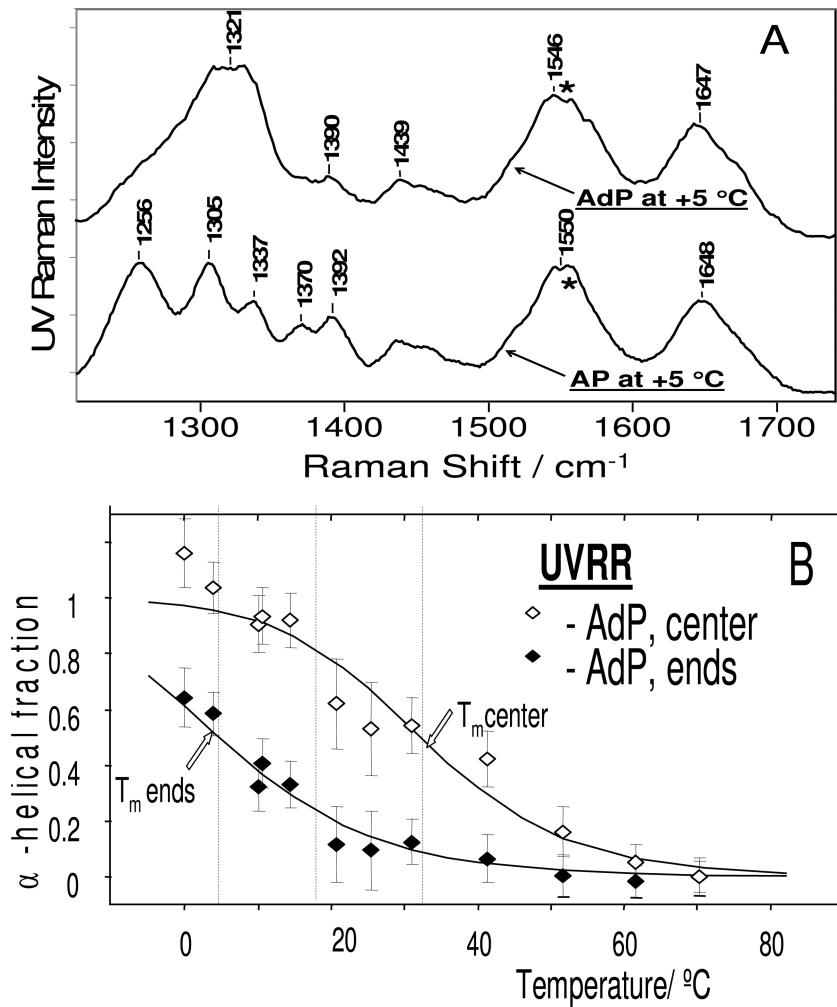


Figure 15.

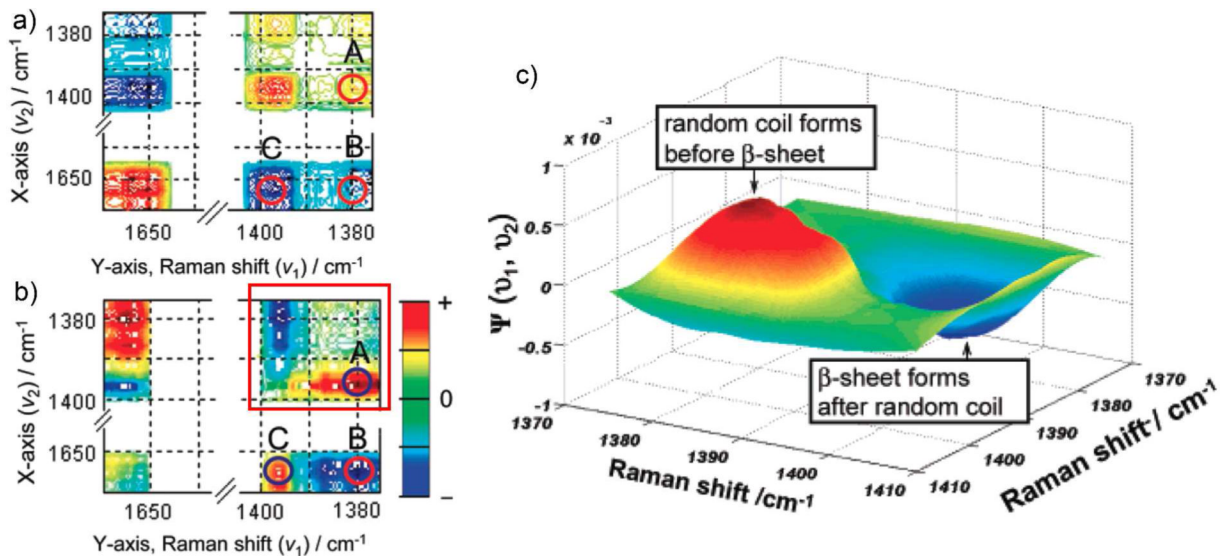
Calculated Ramachandran Ψ probability distributions in AP at (A) 0 °C, (B) 10 °C, (C) 20 °C, (D) 30 °C. Adapted with permission from Reference 111. Copyright 2006 American Chemical Society.

**Figure 16.**

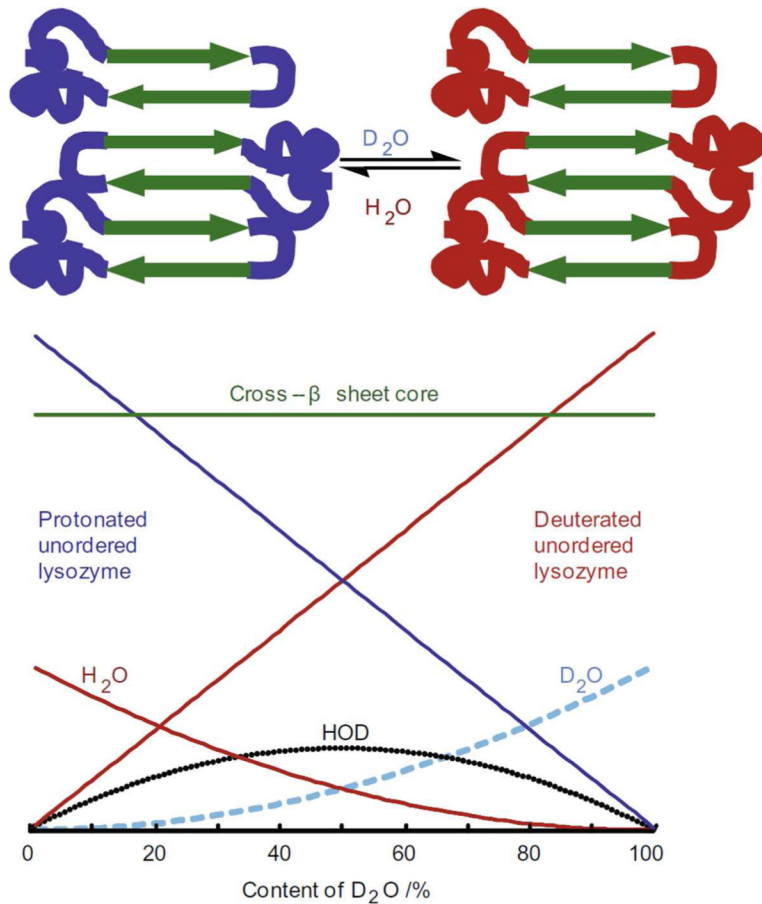
Melting curves for AP “ α -helix-like” conformations. (\times) – Original “ α -helix” melting curve as reported by Lednev et al. (refs. 83 and 98), which is a sum of individual α - π - and 3_{10} -helical melting curves; (\blacklozenge) – Pure α -helix melting; (\blacksquare) – 3_{10} -helix (type III turn) melting; (\bullet) – π -bulge (π -helix) melting. Adapted with permission from Reference 111. Copyright 2006 American Chemical Society.

**Figure 17.**

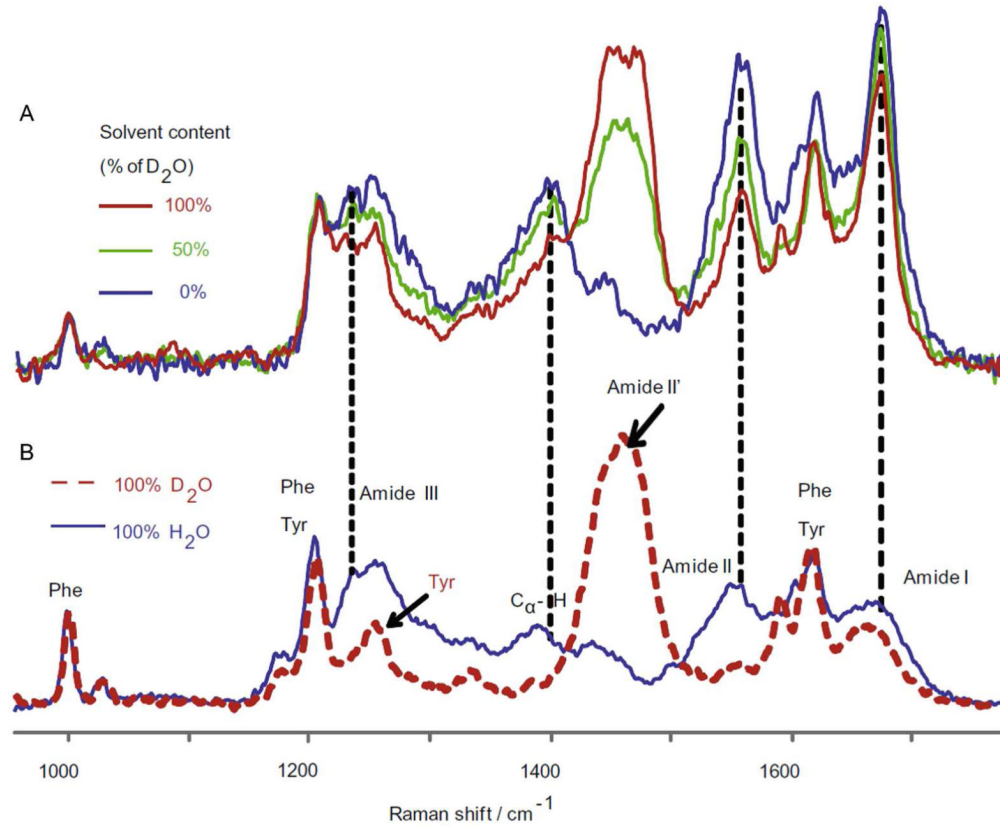
(A) 204 nm UVRR spectra of AdP ($\mathbf{A_dA_dA_dA_dA_dA_dA_d-RAAAAA-R-A_dA_dA_dA_d-R-A_dA_d}$. The bold letters label the 2,3,3,3-deuterated ala residues) and AP (AAAAAAA-RAAAAA-R-AAAAA-R-AA); (B) The temperature dependence of α -helical fractions of the central peptide bonds and exterior peptide bonds normalized to the number of peptide bonds of the central and external segments that can form α -helices. (A) Adapted with permission from Reference 107. Copyright 2007 American Chemical Society. (B) Adapted with permission from Reference 110. Copyright 2002 American Chemical Society.

**Figure 18.**

2D Correlation spectroscopy was used to establish sequential order of events during the fibrillation of hen egg white lysozyme. The synchronous (a) and asynchronous (b) 2D-DUVR correlation maps of the C_α-H bending region and α -helix sub-band of the Amide I region suggest the order of structural change to be: random coil \rightarrow α -helix \rightarrow β -sheet. (Adapted with permission from ref. 125) The 3D perspective plot (c) of the asynchronous C_α-H bending region (red rectangle in (b)) illustrates the implication that random coil forms before β -sheet. (a and b) Adapted with permission from Reference 137. Copyright 2008 American Chemical Society. (c) Adapted with permission from Reference 136. Copyright 2007 American Chemical Society.

**Figure 19.**

Hydrogen-deuterium exchange (HX) was used to allow for the extraction of the Raman signature of the fibril core. (top) Schematic representation of HX: the protonated fibril core is protected from HX, while the unordered fraction is not. (bottom) Expected concentration profile of major components vs. the fraction of D_2O : protonated unordered lysozyme (blue), cross- β -sheet core (green), deuterated unordered lysozyme (red), H_2O (brown solid), HOD (black solid), and D_2O (light blue dashed). Reprinted with permission from Reference 140. Copyright 2010 Elsevier.

**Figure 20.**

Deep UVRR spectral changes in fibrillar and unordered hen egg white lysozyme after hydrogen-deuterium exchange provide evidence of a still-protonated core. (A) DUVRR spectra of HEWL fibrils in H_2O (blue), D_2O (red), and 50/50% $\text{H}_2\text{O}/\text{D}_2\text{O}$ mixture (green). (B) DUVRR spectrum of unordered lysozyme in H_2O (blue), and D_2O (red). Reprinted with permission from Reference 140. Copyright 2010 Elsevier.

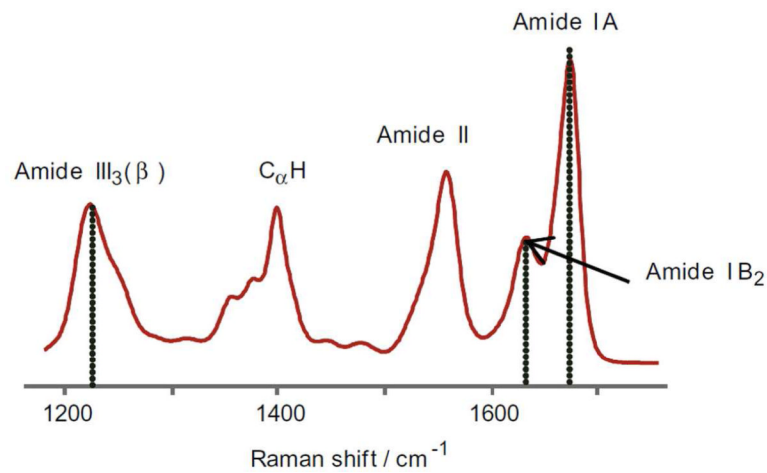


Figure 21.

Deep UVRR spectrum of the cross- β -core of hen egg white lysozyme extracted using Bayesian source separation. Reprinted with permission from Reference 140. Copyright 2010 Elsevier.

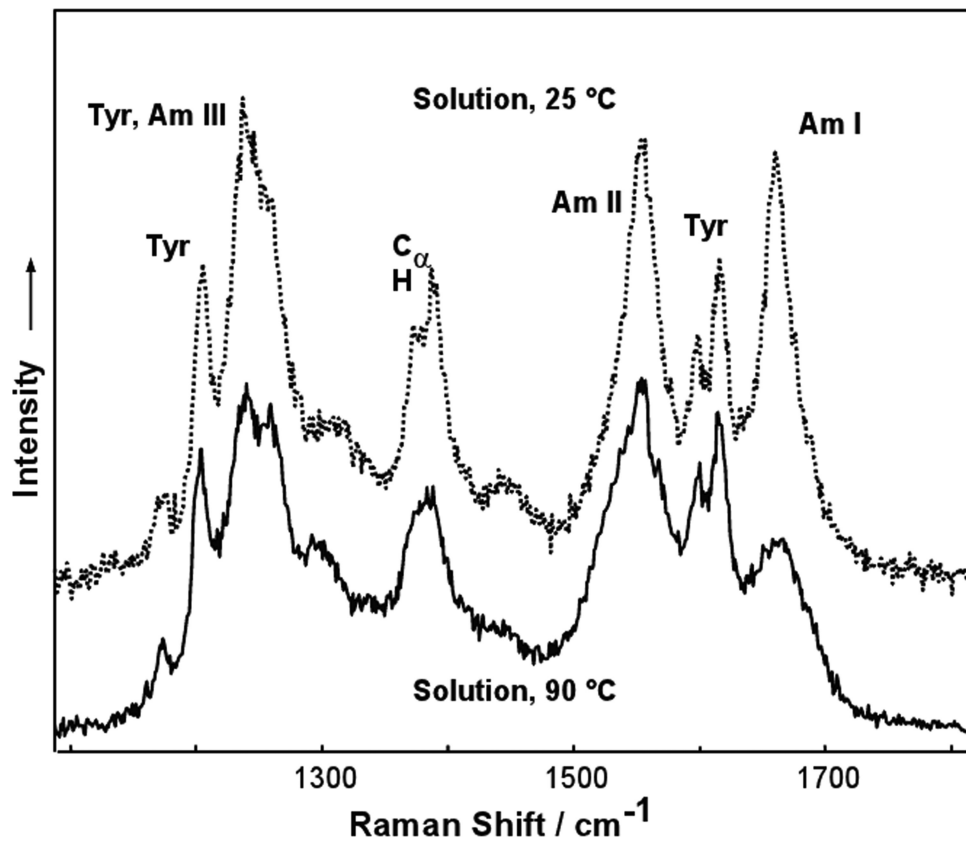


Figure 22.

Deep UVRR spectra of a genetically engineered polypeptide (YEHK21) heated to various temperatures were recorded to detect spectral changes resulting from β -sheet melting. Deep UVRR spectra of YEHK21 in solution at 25 and 90 °C, illustrating spectral differences characteristic of β -sheet melting. Reprinted with permission from Reference 163. Copyright 2006 Elsevier.

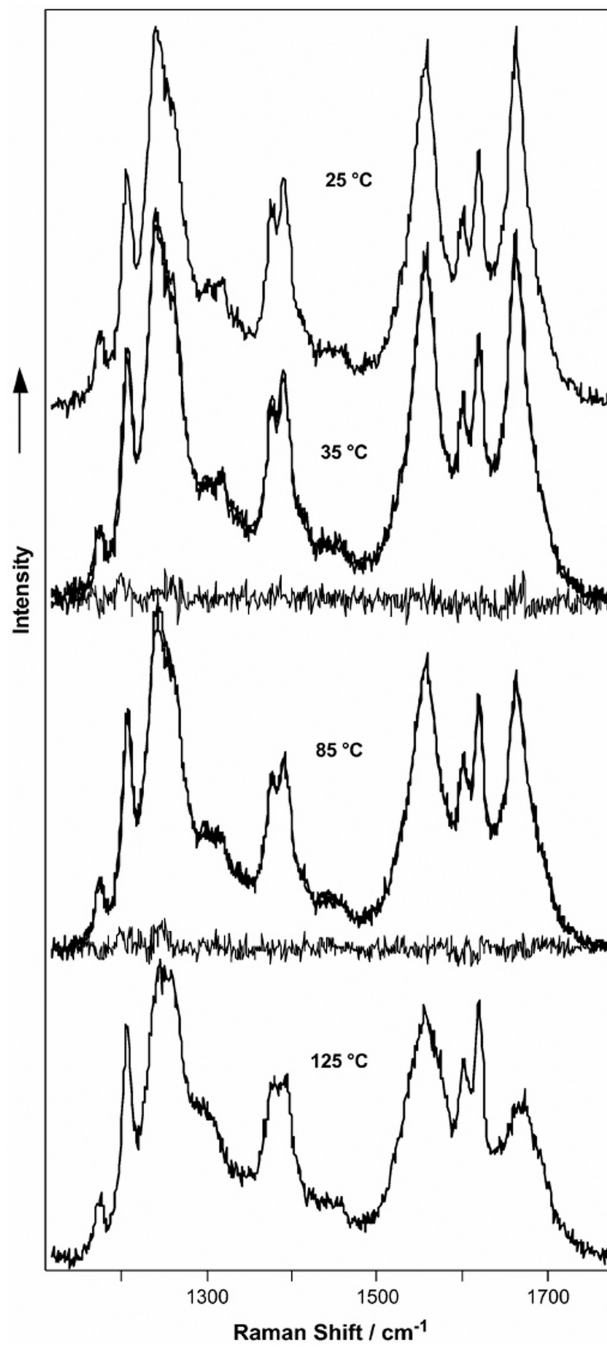


Figure 23.

Due to the temperature dependence of the basis spectra, all measurements had to be recorded at the same temperature to allow for evaluation of conformational changes of the YEHK21 polypeptide. The experimental spectra were fit using basis spectra of completely folded and unordered YEHK21, and tyrosine. Deep UVRR spectra of YEHK21 measured at room temperature after 5 minutes of heating to 35, 85, and 125 °C. Calculated spectra and difference spectra between the measured and calculated ones are shown for 35 and 85 °C. Reprinted with permission from Reference 163. Copyright 2006 Elsevier.

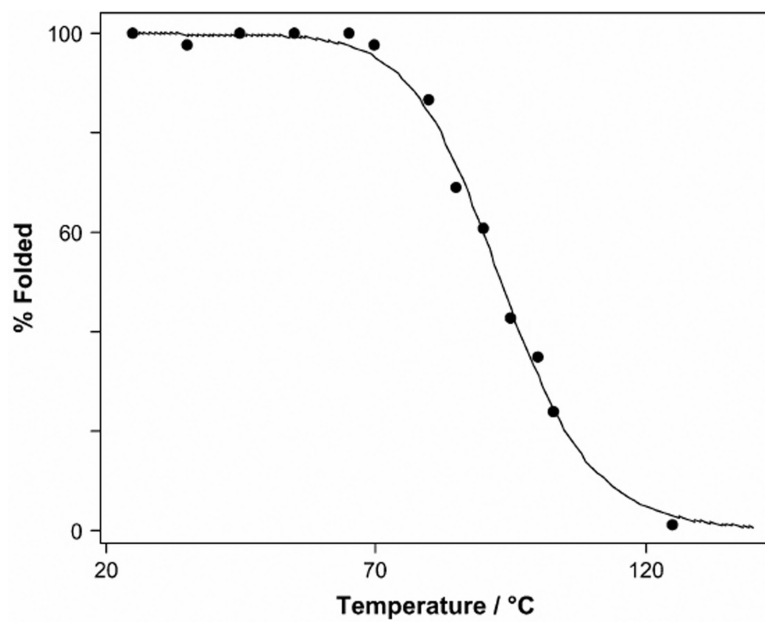
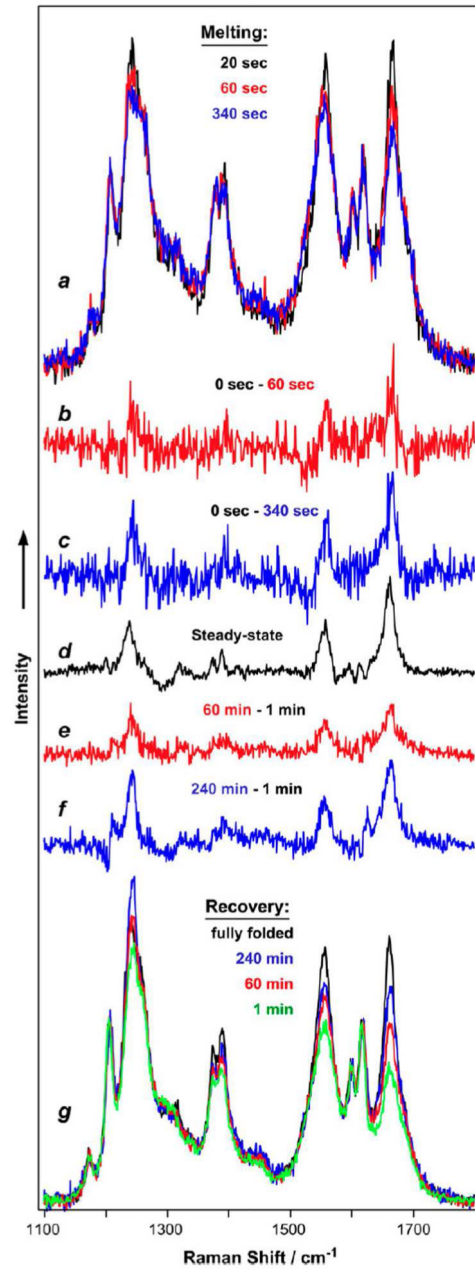


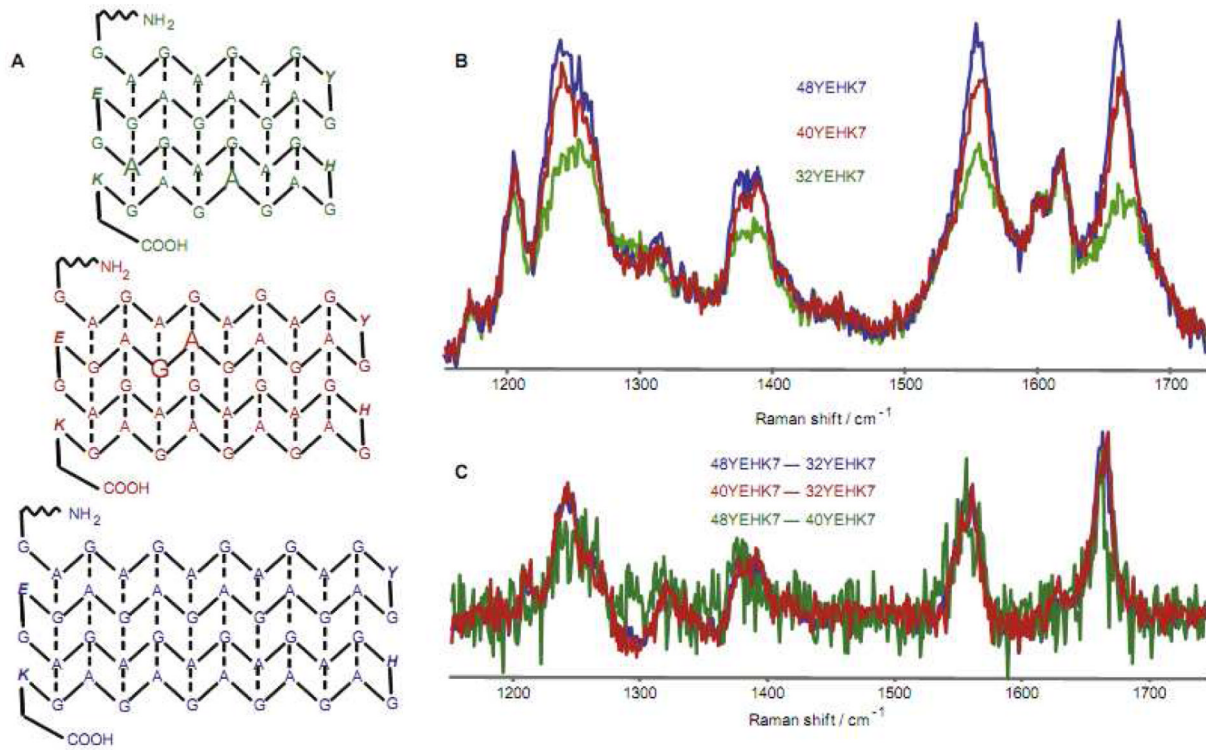
Figure 24.

A YEHK21 melting curve was constructed by plotting the fraction of folded peptide against temperature (solid circles). The solid line represents the best fit for equation (6). Reprinted with permission from Reference 163. Copyright 2006 Elsevier.

**Figure 25.**

Temperature jump measurements were made to assess the kinetics of β -sheet melting, the results of which were quite close to those observed in steady-state measurements. A temperature dependence of the extent of recovery of the starting deep UVRR spectrum was also observed. Deep UVRR spectra of YEHK21 measured at 20, 60, and 340 s after temperature jump (a). Difference spectra of deep UVRR spectrum measured before and 60(b) and 340(c) s after temperature jump. Difference spectrum of deep UVRR spectra of initial folded YEHK21 and that measured at room temperature after being briefly heated to 125°C (d). Difference spectrum of deep UVRR spectra of initial folded YEHK21 subtracted from that measured at room temperature 60(e) and 240(f) minutes after being briefly heated to 100°C. Deep UVRR spectra measured at room temperature 1, 60, and 240 minutes after a

5-minute heating to 100 °C (*g*). Reprinted with permission from Reference 163. Copyright 2006 Elsevier.

**Figure 26.**

Three genetically engineered polypeptides with virtually identical turn contributions were used to establish the first direct measurement of the β -turn Raman signature. The similarities in the difference spectra confirm the validity of this approach. (A) Schematic representation of 32YEHK7, 40YEHK7, and 48 YEHK7 polypeptide amyloid fibril building blocks. (B) Deep UVRR spectra and (C) difference spectra of 32YEHK7, 40YEHK7, and 48 YEHK7. Adapted with permission from Reference 140. Copyright 2008 American Chemical Society.

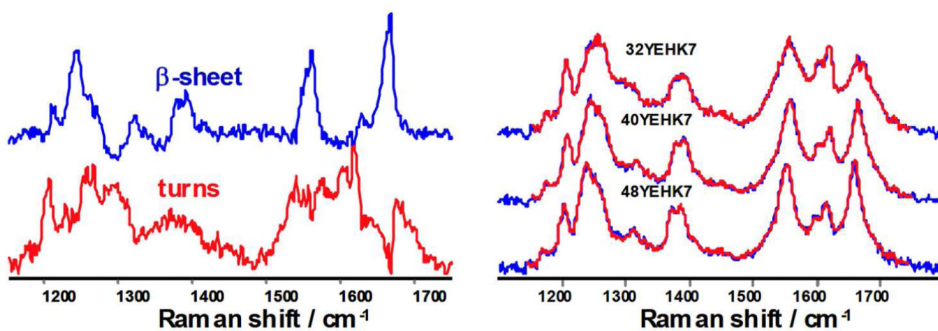
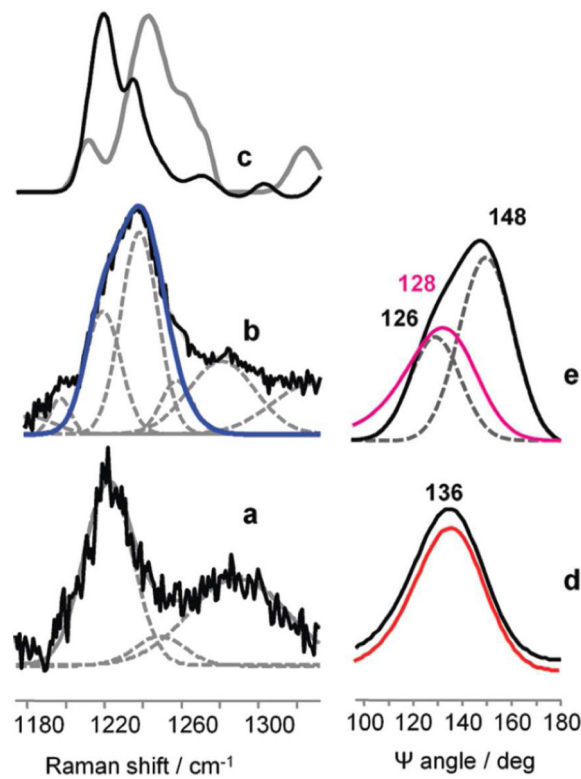


Figure 27.

The deep UVRR spectral signatures of YEHK polypeptide β -sheet and turns fit the experimental spectra with close agreement, indicating that these peptides are composed primarily of these two structures. Deep UVRR spectra of β -sheet and turns (left), and the deep UVRR spectra of YEHK fibrils fitted with a linear combination of these two components (right). Adapted with permission from Reference 141. Copyright 2008 American Chemical Society.

**Figure 28.**

Solid-State NMR data of $\text{A}\beta_{1-40}$ fibrils were used to verify the applicability of the Asher group's Ψ distribution method to quantitatively characterize the fibril core conformation of peptides using deep UVRR spectroscopy. (a) Deep UVRR spectra of the $\text{A}\beta_{34-42}$ fibril core (solid line) and the best fit with Gaussian peaks (dotted lines); (b) Deep UVRR spectra of the $\text{A}\beta_{1-40}$ fibril core (solid line) and the best fit with Gaussian peaks (dotted lines) and the calculated spectrum based on SSNMR data (blue line); (c) hamster prion protein (black) and YEHK peptide (grey); (d) Ψ angle distribution in the $\text{A}\beta_{34-42}$ fibril core (black) and average antiparallel β -sheets in globular proteins; (e) calculated Ψ angle distribution in the $\text{A}\beta_{1-40}$ fibril core (black), the best fit with Gaussian curves (dashed lines), and the Ψ angle distribution in average parallel β -sheets in globular proteins (pink). Adapted with permission from Reference 135. Copyright 2010 American Chemical Society.

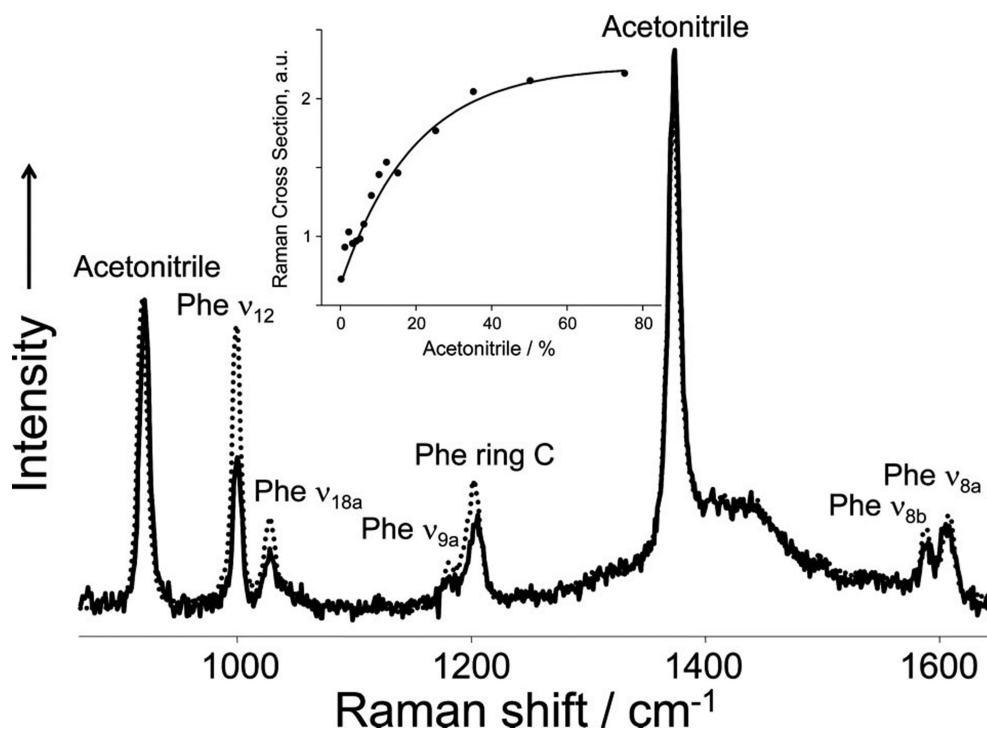
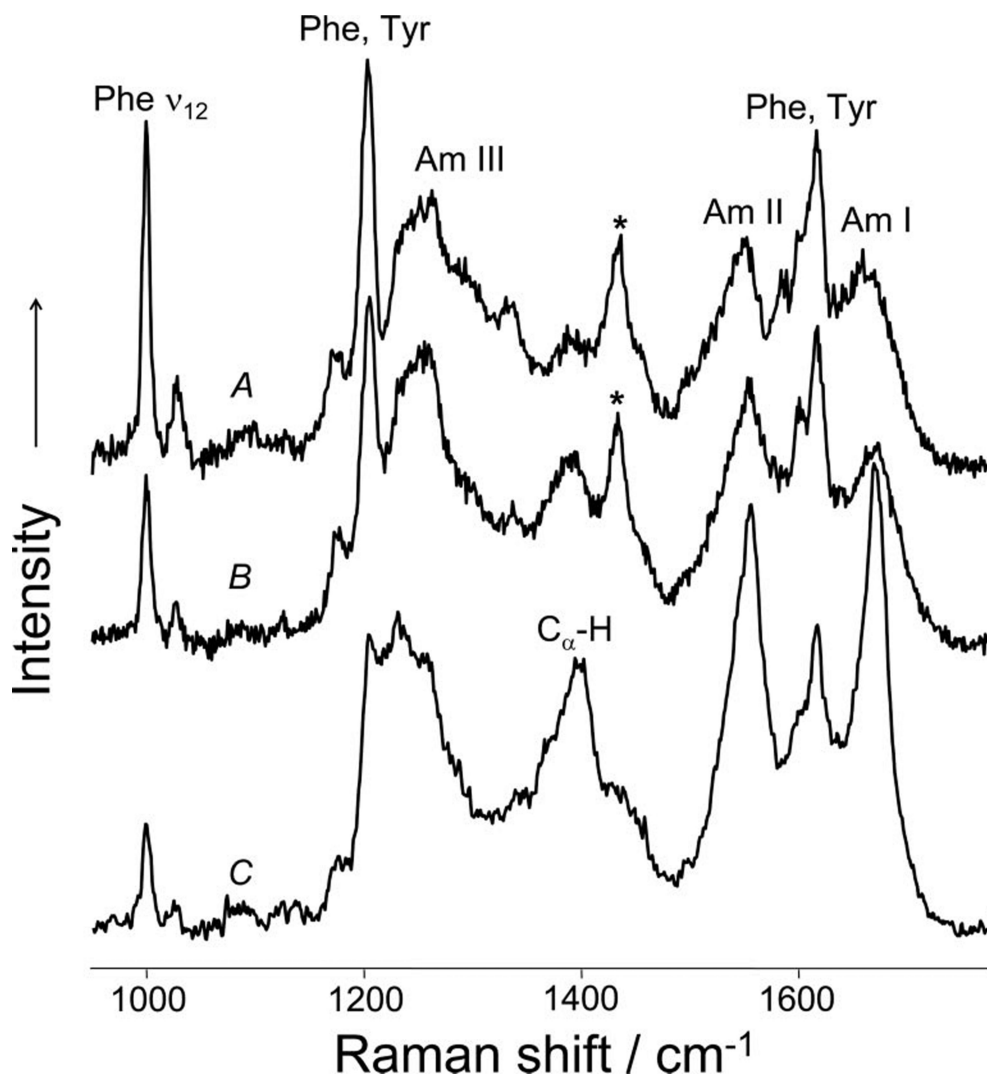


Figure 29.

The Raman cross-section of the 1000 cm^{-1} band phenylalanine band was shown to vary as a function of water exposure, making it a useful probe of local environment. Deep UV Resonance Raman spectra of *N*-acetyl-L-phenylalanine ethyl ester in water and 50% acetonitrile (dotted line) and 5% acetonitrile (solid line). Inset: Raman cross section of the 1000 cm^{-1} band as a function of acetonitrile concentration. Reprinted with permission from Reference 133. Copyright 2008 American Chemical Society.

**Figure 30.**

Deep UV Resonance Raman spectra of hen egg white lysozyme were recorded at various times of incubation. Not incubated (A), soluble phase after 2 days of incubation (B), and the gelatinous phase (C). * is the internal standard peak. Reprinted with permission from Reference 133. Copyright 2008 American Chemical Society.

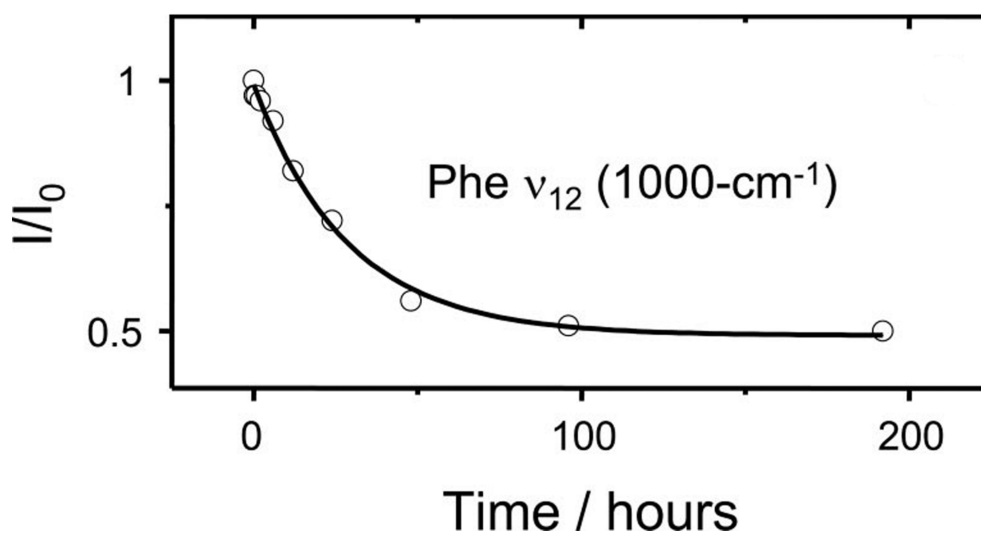


Figure 31.

The local environment of hen egg white lysozyme was probed using phenylalanine as an intrinsic reporter. The relative intensities of the 1000 cm^{-1} bands of phenylalanine from the Raman spectra of HEWL were plotted as a function of incubation time, indicating an increasing exposure of phenylalanine to water as fibrillation progresses. Reprinted with permission from Reference 133. Copyright 2008 American Chemical Society.

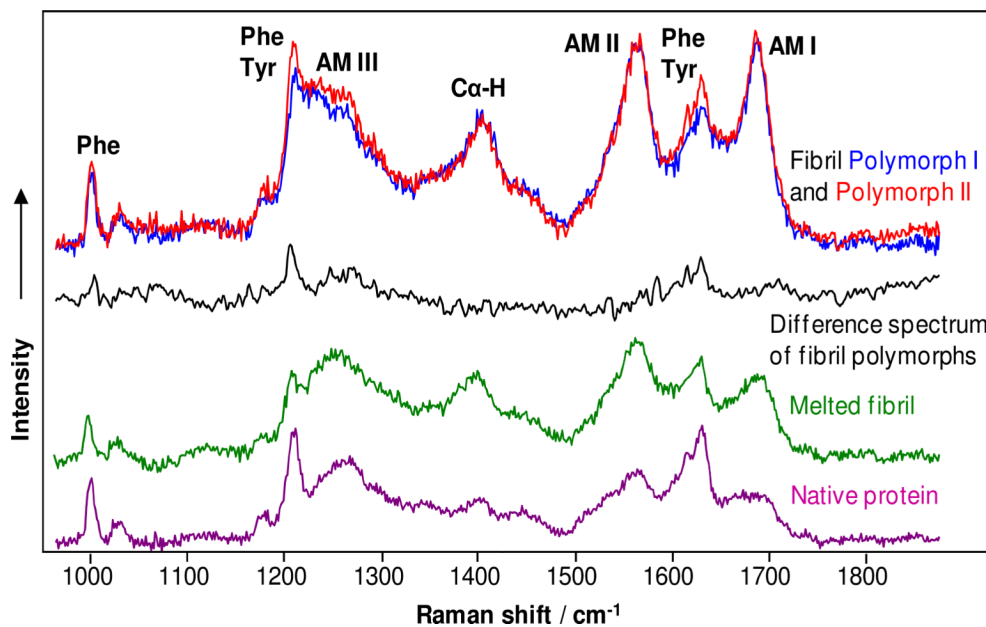


Figure 32.

Spontaneous refolding of apo- α -lactalbumin fibrils from one polymorph to another after the temperature is dropped by 12 °C and the solution was desalting. DUVRR spectra of native apo- α -lactalbumin, fibril Polymorph I (prepared at 37 °C), partially melted fibrils after 5 hours of incubation at 25 °C, and fibril Polymorph II (after 8 h of incubation at 25 °C). Reprinted with permission from Reference 172. Copyright 2010 Royal Society of Chemistry.

Table 1

Identifying the possible types of one- or two-step reaction mechanism based on the intensities of synchronous and asynchronous 2D correlation maps. Adapted with permission from Reference 137. Copyright 2008 American Chemical Society.

Observation		
Intensities on synchronous map	Intensities on asynchronous map ^a	Possible mechanism
A and B negatively correlated	A and B are synchronous	$A \rightarrow B$ or $A \rightleftharpoons B$
A and B are negatively correlated at all stages of the reaction	B changes before A	$A \rightarrow B \rightleftharpoons P$ or $A \rightleftharpoons B \rightleftharpoons P$
Correlation of A and B changes sign over the course of the reaction ^b	Sequential order $A \rightarrow P \rightarrow B$ or $B \rightarrow A \rightarrow P$	$A \rightarrow B \rightarrow P$ or $A \rightleftharpoons B \rightarrow P$

^aSequential order may change when varying the ratios of rate constants. Simulations using anticipated rate constants are advised when testing for all mechanisms.

^bThis can also be the case for the reaction $A \rightleftharpoons B \rightleftharpoons P$ and $A \rightarrow B \rightleftharpoons P$.

Table 2

Characteristic times for transformations of native lysozyme to partially unfolded intermediate (τ_1), partially unfolded intermediate to nucleus (τ_2), and nucleus to partially unfolded intermediate (τ_{-2}) for three concentrations. Adapted with permission from Reference 136. Copyright 2007 American Chemical Society.

Concentration mg/mL	Characteristic time, hours		
	τ_1	τ_2	τ_{-2}
70	30±2	70±20	15±5
14	30±2	70±10	12±3
1.4	30±2	74±16	14±5